Cross-correlation search for continuous gravitational waves from a compact object in SNR 1987A in LIGO Science run 5

L. Sun,[1,*] A. Melatos,[1,†] P. D. Lasky,[2,1] C. T. Y. Chung,[1] and N. S. Darman[1]

[1]*School of Physics, University of Melbourne, Parkville, VIC 3010, Australia*

[2]*Monash Centre for Astrophysics, School of Physics and Astronomy, Monash University, Clayton, VIC 3800, Australia*

(Received 7 April 2016; published 19 October 2016)

We present the results of a cross-correlation search for gravitational waves from SNR 1987A using the second year of LIGO science run 5 data. The frequency band 75–450 Hz is searched. No evidence of gravitational waves is found. A 90% confidence upper limit of $h_0 \leq 3.8 \times 10^{-25}$ is placed on the gravitational-wave strain at the most sensitive frequency near 150 Hz. This corresponds to an ellipticity of $\epsilon \leq 8.2 \times 10^{-4}$ and improves on previously published strain upper limits by a factor of approximately 4. We perform a comprehensive suite of validations of the search algorithm and identify several computational savings that marginally sacrifice sensitivity in order to streamline the parameter space being searched. We estimate detection thresholds and sensitivities through Monte Carlo simulations.

DOI: 10.1103/PhysRevD.94.082004

I. INTRODUCTION

Neutron stars in young supernova remnants are excellent targets for ground-based gravitational-wave interferometers such as the Laser Interferometer Gravitational Wave Observatory (LIGO). Young neutron stars may be more promising targets than their older counterparts for three reasons. First, searches for periodic gravitational waves from younger neutron stars can more easily reach or probe below the indirect upper limits inferred from the spin-down rate $\dot{\nu}$ (where $\dot{\nu}$ is measured) or the age (where $\dot{\nu}$ is unknown). Indirect wave strain upper limits are proportional to $\dot{\nu}$ or inversely proportional to the age and hence are larger for younger neutron stars [1–3]; see also Eq. (1) in Sec. II B. Second, less time has passed in young objects for their crusts and interiors to settle down and erase historical nonaxisymmetries frozen-in at birth. Third, young objects spin down rapidly, driving crust-superfluid differential rotation, which can excite nonaxisymmetric flows in the high-Reynolds-number interior [4–6]. For a review of gravitational-wave generation mechanisms in neutron stars, see Refs. [1,7]. On the other hand, even if young neutron stars strongly emit gravitational waves, their rapid spin-down is a disadvantage for detection because the phase of the gravitational-wave signal evolves rapidly. A prohibitively large set of matched filters is needed for a coherent search, if a radio ephemeris is unavailable [8]. Hence less-sensitive semicoherent search strategies are favored [3,9–13].

LIGO achieved its design sensitivity over a wide band during its fifth and sixth science runs (S5 [14] and S6 [15], respectively). Data from S5 and S6 have been analyzed in several searches for continuous-wave sources in supernova remnants targeting specific, known sources like the Crab pulsar [16–18], Cassiopeia A [19,20], other young pulsars with radio or x-ray ephemerides [18,21], and young supernova remnants [22]. Broadband, all-sky searches have also been carried out for unknown sources, some of which may turn out post-discovery to reside in supernova remnants [23–25]. Although no detections resulted from these searches, upper limits have been placed on parameters of astrophysical interest, e.g., the maximum ellipticity and internal magnetic field strength of the Crab pulsar [16,17] and the amplitude of r-mode oscillations in Cassiopeia A [20].

In this paper, we report on the search for periodic gravitational waves from a possible neutron star in one of the youngest and closest known supernova remnants, SNR 1987A. The remnant was produced by a type-II core-collapse supernova, which occurred in February 1987 in the Large Magellanic Cloud (right ascension $\alpha = 5$ h 35 m 28.03 s, declination $\delta = -69°\ 16'\ 11.79''$, distance $d = 51.4$ kpc); see reviews by Panagia [26] and Immler *et al.* [27]. The gravitational-wave search relies on the semi-coherent cross-correlation algorithm [12], which has also been used in searches for gravitational waves from the low-mass x-ray binary Sco X-1 [28,29]. Although the noise power spectral density of the LIGO S5 run is higher than that of the first Advanced LIGO observation run (O1), there are strong reasons to look for gravitational waves from SNR 1987A in the earlier data set. For example, the S5 run is considerably longer than O1, and the expected gravitational-wave amplitude during S5 is larger than during O1, given that the neutron star has aged significantly in the intervening ten years, which amounts to 35% of the object's age.

The structure of the paper is as follows. In Sec. II, we discuss the evidence for a neutron star in SNR 1987A and

*lings2@student.unimelb.edu.au
†amelatos@unimelb.edu.au

briefly review the results of previous gravitational-wave searches. Section III summarizes the theory and implementation of the cross-correlation algorithm and the associated astrophysical phase model. Section IV reports on the verification tests performed on synthetic data containing pure noise and injected signals and evaluates the sensitivity penalty exacted when averaging over source orientation and polarization in order to reduce computational cost. In Sec. V, we calculate the sensitivity of the search as a function of the frequency and spin-down rate. Section VI presents the results obtained from running the search on LIGO S5 data and interprets the results astrophysically.

II. A NEUTRON STAR IN SNR 1987A?

A. Indirect evidence for formation

No neutron star has yet been detected electromagnetically in SNR 1987A, either reproducibly as a pulsar or as a nonpulsating central compact object [30]. Nevertheless, strong theoretical evidence exists for the existence of a neutron star in SNR 1987A from detailed studies of the progenitor (see, e.g., Refs. [31,32]) and the coincident worldwide detection of core-collapse neutrinos from the supernova event [33–36]. Although no pulsar detection has been confirmed, numerous searches have placed upper limits on the flux and luminosity at radio (<115 μJy at 1390 MHz; see Ref. [27]), optical/near-UV ($<8\times10^{33}$ ergs s^{-1}; see Ref. [37]), and soft x-ray ($<2.3\times10^{34}$ erg s^{-1}; see Ref. [38]) wavelengths. Middleditch *et al.* [39] reported finding an optical pulsar in SNR 1987A with a frequency of 467.5 Hz, modulated sinusoidally with a period of about 1 ks, consistent with precession given an ellipticity of $\epsilon\sim10^{-6}$. The pulsations disappeared after 1996 [39] and were never confirmed independently.

One possible reason why a pulsar has not yet been detected is that its magnetic field is too weak. The weak-field theory is supported by some theoretical models, in which the field grows after the neutron star is formed over about 10^3 yr, e.g., due to thermomagnetic effects [40–42]. In a related scenario, the magnetic field of a millisecond pulsar intensifies (linearly or exponentially) from about 10^{10} G at birth to about 10^{12} G after around 0.3–0.7 kyr, before the pulsar spins down significantly [43]. On the other hand, the neutron star may be born with a strong magnetic field, which is amplified during the first few seconds of its life by dynamo action (see, e.g., Refs. [44,45]). Population synthesis calculations combined with measurements of the known spin periods of isolated radio pulsars imply a distribution of birth magnetic field strengths B_0 satisfying $\log B_0 = 12.65\pm0.55$ (1σ range) [46–48]. Several birth scenarios for the pulsar in SNR 1987A were considered by Ögelman and Alpar [49] in this context, who concluded that the maximum magnetic dipole moment is 1.1×10^{26} G cm^3, 2.5×10^{28} G cm^3, and 2.5×10^{30} G cm^3 for birth periods of 2 ms, 30 ms, and 0.3 s, respectively. The dynamo model also accommodates a magnetar in SNR 1987A, with a magnetic dipole moment exceeding 2.4×10^{34} G cm^3, regardless of the initial spin period [49].

Estimates of the birth spin of the putative pulsar in SNR 1987A are more uncertain. Simulations of the bounce and postbounce phases of core collapse produce proto-neutron star spin periods between 4.7 ms and 140 ms, proportional to the progenitor's spin period [50]. Some population synthesis studies, which infer the radio pulsar velocity distribution from large-scale 0.4-GHz pulsar surveys, favor shorter millisecond birth spin periods [47], while others argue the opposite (300 ± 150 ms; 1σ range) [48]. Faint, nonpulsed, x-ray emission from SNR 1987A was first observed four months after the supernova, and it decreased steadily in 1989 [51,52], leading to the suggestion that a neutron star could be powering a plerion, which is partially obscured by a fragmented supernova envelope. A model of the plerion's x-ray spectrum, with a magnetic field of 10^{12} G and an expansion rate of 5×10^8 cm s^{-1}, fits the x-ray data for a pulsar spin period of 18 ms.

Despite their indirect nature, the above studies broadly justify a search for gravitational waves from SNR 1987A at frequencies from about 50 Hz to 450 Hz (i.e., twice the spin frequency), bracketing the most sensitive portion of the LIGO band. The range of frequency derivative searched in this paper, namely, from 10^{-13} Hz s^{-1} to 10^{-6} Hz s^{-1}, is consistent with a magnetic field between 10^9 G and 10^{12} G at the present epoch and hence with the B_0 values above. It is also consistent with maximum ellipticity in the range $10^{-5}\lesssim\epsilon\lesssim10^{-4}$, if the spin-down is gravitational-wave dominated.

B. Indirect gravitational radiation limits

Neither ν nor $\dot{\nu}$ is known for the putative neutron star in SNR 1987A, so one is unable to infer an indirect spin-down upper limit on the characteristic wave strain h_0 by assuming that all the observed spin-down luminosity $4\pi^2 I\nu\dot{\nu}$ (where I is the stellar moment of inertia) goes into gravitational radiation [3,19]. However, by a similar energy conservation argument, one can place an upper limit on h_0 in terms of the object's age, $T_{\rm age}$ [3,8,20], viz.

$$h_0 \le \frac{1}{D}\left(\frac{5GI|\xi|}{2c^3T_{\rm age}}\right)^{1/2}, \tag{1}$$

with

$$\xi = \frac{1}{n-1}\left[1-\left(\frac{\nu_b}{\nu}\right)^{1-n}\right], \tag{2}$$

where G is Newton's gravitational constant, c is the speed of light, D is the distance to the source, n is the braking index defined via $\dot{\nu}\propto\nu^n$ (assumed to be constant here, for simplicity), ν_b is the spin frequency at birth, and

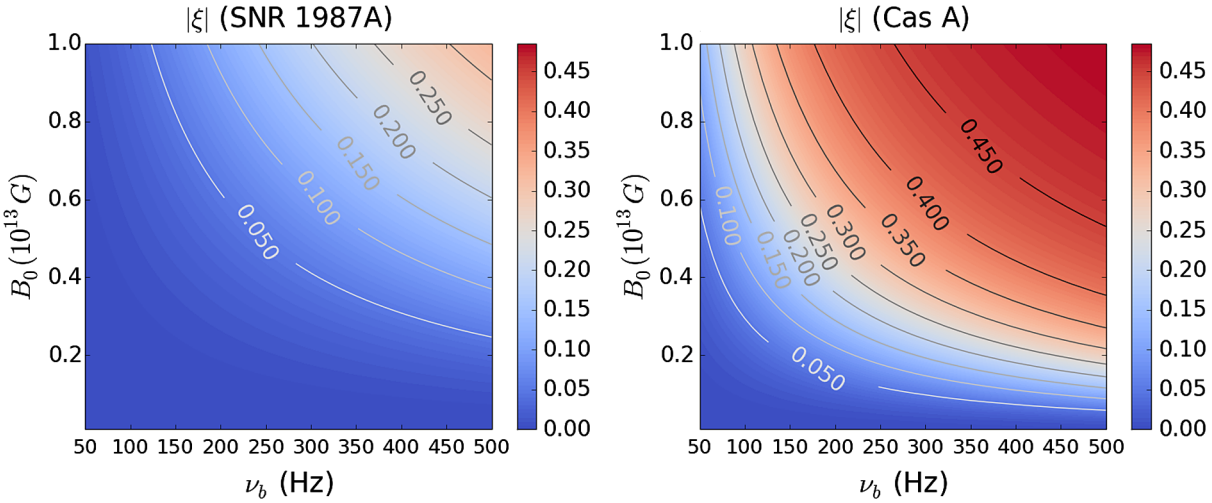

FIG. 1. Contours of age factor $|\xi|$ in Eq. (2) for SNR 1987A (left panel) and Cas A (right panel) as a function of the spin frequency at birth ν_b and dipole magnetic field B_0 with $n = 3$.

$|\xi|^{-1}T_{\rm age} = -\nu/\dot{\nu}$ is proportional to the characteristic electromagnetic spin-down time scale [19].

The factor $|\xi|$ in Eq. (1) is normally neglected when quoting indirect limits under the assumption $\nu \ll \nu_b$ [8,20]. This assumption is reasonable for objects like Cas A but not for SNR 1987A, where $T_{\rm age}$ is much less than $-\nu/\dot{\nu}$ for many reasonable choices of birth spin and magnetic field [53]. Figure 1 illustrates this point. It displays contours of $|\xi|$ as a function of ν_b and dipole magnetic field B_0, assuming purely electromagnetic spin-down ($\dot{\nu} \propto B_0^2\nu^n$, $n = 3$), for simplicity. The spin-down model is described in more detail in Sec. III B. The left-panel contours (SNR 1987A; $T_{\rm age} = 19$ yr) satisfy $|\xi| \ll 1$ except in the top-right corner of the plot (e.g., $\nu_b \gtrsim 350$ Hz, $B_0 \gtrsim 7 \times 10^{12}$ G for $|\xi| \gtrsim 0.25$). By contrast, the right-panel contours (Cas A; $T_{\rm age} \simeq 333$ yr) satisfy $|\xi| \gtrsim 0.25$ over more of the plot, as befits an older object with $\nu \ll \nu_b$.

The indirect upper limit on h_0 is inversely proportional to $T_{\rm age}$. Hence it is harder to reach observationally for older neutron stars. Younger objects like the putative neutron star in SNR 1987A generally have a higher limit on h_0, although not as high as one would expect assuming $\dot{\nu} \approx \nu T_{\rm age}^{-1}$ in view of the "ξ effect" discussed above. The fact that young neutron stars with $\nu \approx \nu_b$ spin-down slower than $\sim\nu T_{\rm age}^{-1}$ aids detection by dramatically reducing the number of matched filters required to track the phase evolution. The latter advantage is further discussed in Sec. IV D 3.

C. Previous gravitational-wave searches

The likely existence of a young neutron star in SNR 1987A makes it a good target for gravitational-wave searches [54,55]. A coherent matched-filtering search was carried out in 2003 with the TAMA 300 detector, searching 1.2×10^3 hours of data from its first science run over a 1-Hz band centered on 934.9 Hz, assuming a spin-down range of $(2\text{–}3) \times 10^{-10}$ Hz s^{-1}. The search yielded an upper limit on the wave strain of $h_0 \leq 5 \times 10^{-23}$ [56]. An earlier matched-filtering search was conducted using 10^2 hours of data taken in 1989 by the Garching prototype laser interferometer. The latter search was carried out over 4-Hz bands near 2 kHz and 4 kHz; it did not include any spin-down parameters, and it yielded a strain upper limit of $h_0 \leq 9 \times 10^{-21}$ [57].

The most sensitive gravitational-wave search to date for SNR 1987A was conducted with the radiometer pipeline using LIGO S5 data [58]. This search yielded an upper limit on the wave strain of $h_0 \approx 1.57 \times 10^{-24}$ (90% confidence level) in the most sensitive frequency range near 160 Hz. It is noted that the radiometer analysis always assumes a circularly polarized signal, so in a case of random polarization like the one discussed in this paper, the equivalent radiometer strain upper limit needs to be converted to a more conservative value, by multiplying a sky-position-dependent factor of 2.248 [59]. The above upper limit $h_0 \approx 1.57 \times 10^{-24}$ has already been converted from the original value stated in Ref. [58].

A coherent search for SNR 1987A based on the optically derived spin parameters of Middleditch *et al.* [39] requires 30 days of integration time and at least 10^{19} search templates covering just the frequency and its first derivative [60]. Of course, the optical detection has not been confirmed independently, so one may have $\nu \ll 467.5$ Hz in reality, reducing $\dot{\nu} \propto \nu^3$ and hence the number of templates. Nevertheless, as a rule, young objects do spin down rapidly, and typically five or six higher-order frequency derivatives must be searched in order to accurately track the gravitational-wave phase. In order to sidestep this problem, Chung *et al.* [8] proposed an astrophysically motivated phase model that describes the spin-down in terms of the

ellipticity, magnetic field, and electromagnetic braking index of the source instead of its frequency derivatives. The model is most useful if the braking index varies slowly during the observation, in a sense that will be defined precisely in Sec. IV D 3. At the time of writing, it was unclear, on astrophysical grounds, whether a slowly varying braking index is favored or disfavored by theoretical arguments (e.g., Refs. [61,62]) and the sparse observational data available [63].

III. SEARCH PIPELINE

A. Cross-correlation algorithm

The theoretical basis of the cross-correlation algorithm was described in detail by Dhurandhar *et al.* [12]. Here, we briefly summarize the key results that are necessary for the algorithm's implementation.

The algorithm operates on interferometer data in the form of short Fourier transforms (SFTs) [3], usually of 30-min duration. It outputs a cross-correlation detection statistic called the ρ statistic. SFTs are multiplied pairwise according to some criterion (e.g., time lag or interferometer combination) to form a raw cross-correlation variable

$$\mathcal{Y}_{IJ} = \frac{\tilde{x}^*_{k_I,I}\tilde{x}_{k_J,J}}{(\Delta T)^2}, \tag{3}$$

where I and J index the pair of SFTs $\tilde{x}_{k_I,I}$ and $\tilde{x}_{k_J,J}$; k_I and k_J are the indices of the frequency bins of the two SFTs; and ΔT denotes the length of the SFTs. The gravitational-wave signal is assumed to be concentrated in a single-frequency bin in each SFT, i.e., $\Delta T \ll \nu/\dot{\nu}$ due to sidereal motion and pulsar spin-down.

The frequency range spanned by the two SFTs is the same, but the signal does not appear in the same frequency bin in $\tilde{x}_I$ and $\tilde{x}_J$. The specific frequency bins with indices k_I and k_J multiplied in Eq. (3) are related by the time lag between the pair and between interferometers, as well as spin-down and Doppler effects. For an isolated source, the instantaneous signal frequency at time t is given by

$$\nu(t) = \hat{\nu}(t)\left(1 + \frac{\mathbf{v}\cdot\mathbf{n}}{c}\right), \tag{4}$$

where $\hat{\nu}(t)$ is the instantaneous signal frequency in the rest frame of the source, $\mathbf{v}$ is the detector velocity relative to the source, and $\mathbf{n}$ is the unit vector pointing from the detector to the source. The instantaneous signal frequencies in SFTs I and J, $\nu(T_I)$ and $\nu(T_J)$, are calculated at the times corresponding to the midpoints of the SFTs, T_I and T_J. The frequency bin k_J is therefore shifted from k_I by an amount $\lfloor \Delta T[\nu(T_J) - \nu(T_I)] \rfloor$, where $\lfloor \ldots \rfloor$ denotes the largest integer smaller than $(\ldots)$ [12]. For convenience, we henceforth drop the subscripts k_I and k_J.

The ρ statistic comprises a weighted sum of $\mathcal{Y}_{IJ}$ over all pairs (I, J). The relative weights of the pairs in the ρ statistic are controlled by the polarization amplitudes and phase of the signal and the interferometer antenna pattern. These variables are packaged within the signal cross-correlation function $\tilde{\mathcal{G}}_{IJ}$, defined as

$$\begin{aligned}\tilde{\mathcal{G}}_{IJ} = \frac{1}{4}&\exp(-i\Delta\Phi_{IJ})\exp\{-i\pi\Delta T[\nu(T_I) - \nu(T_J)]\} \\ &\times [F_{I+}F_{J+}\mathcal{A}_+^2 + F_{I\times}F_{J\times}\mathcal{A}_\times^2 \\ &- i(F_{I+}F_{J\times} - F_{I\times}F_{J+})\mathcal{A}_+\mathcal{A}_\times].\end{aligned} \tag{5}$$

In Eq. (5), we define $\Delta\Phi_{IJ} = \Phi_I(T_I) - \Phi_J(T_J)$, where $\Phi_I(T_I)$ is the signal phase at time T_I. The terms in the second set of square brackets in Eq. (5) depend on the polarization angle ψ, and the inclination angle ι between $\mathbf{n}$ and the rotation axis of the pulsar, according to

$$\mathcal{A}_+ = \frac{1}{2}(1 + \cos^2\iota), \tag{6}$$

$$\mathcal{A}_\times = \cos\iota, \tag{7}$$

$$F_+(t;\mathbf{n},\psi) = a(t;\mathbf{n})\cos 2\psi + b(t;\mathbf{n})\sin 2\psi, \tag{8}$$

$$F_\times(t;\mathbf{n},\psi) = b(t;\mathbf{n})\cos 2\psi - a(t;\mathbf{n})\sin 2\psi. \tag{9}$$

Here, $a(t;\mathbf{n})$ and $b(t;\mathbf{n})$ are the detector response functions for a given sky position, defined in Eqs. (12) and (13) of Jaranowski *et al.* [64]. A geometrical definition is also given by Prix and Whelan [65]. The gravitational-wave strain tensor is

$$\overleftrightarrow{h}(t) = h_0[\mathcal{A}_+\cos\Phi(t)\overleftrightarrow{e}_+ + \mathcal{A}_\times\sin\Phi(t)\overleftrightarrow{e}_\times], \tag{10}$$

where h_0 is the characteristic gravitational-wave strain, and $\overleftrightarrow{e}_{+,\times}$ are the basis tensors for the plus (+) and cross (×) polarizations in the transverse-traceless gauge.[1]

With the above definitions, the ρ statistic is given by the weighted sum

$$\rho = \Sigma_{IJ}(u_{IJ}\mathcal{Y}_{IJ} + u^*_{IJ}\mathcal{Y}^*_{IJ}), \tag{11}$$

where the weights are defined by

$$u_{IJ} = \tilde{\mathcal{G}}^*_{IJ}/\sigma^2_{IJ}, \tag{12}$$

and

$$\sigma^2_{IJ} = S_n^{(I)}(\nu_I)S_n^{(J)}(\nu_J)/(4\Delta T^2) \tag{13}$$

is the variance of $\mathcal{Y}_{IJ}$ in the absence of a signal, where $S_n^{(I)}(\nu_I)$ is the power spectral density of SFT I at frequency $\nu_I = \nu(T_I)$. For each frequency and sky position searched,

[1]We alert the reader to an error in Eq. (3.10) of Dhurandhar *et al.* [12], which omits the factor of $\exp\{-i\pi\Delta T[\nu(T_I) - \nu(T_J)]\}$ arising from the choice of time origin of the Fourier transforms. Also see Whelan *et al.* [28].

we obtain *one* real value of ρ, which is a sum of the Fourier power from all the pairs. Ignoring self-correlations (i.e., no SFT is paired with itself), the mean of ρ is predicted to satisfy

$$\mu_\rho = h_0^2 \sum_{IJ} |\tilde{\mathcal{G}}_{IJ}|^2 / \sigma_{IJ}^2. \tag{14}$$

In the limit of zero signal, the variance of ρ is

$$\sigma_\rho^2 = 2 \sum_{IJ} |\tilde{\mathcal{G}}_{IJ}|^2 / \sigma_{IJ}^2. \tag{15}$$

In the presence of a strong signal, and if self-correlations are included, μ_ρ and σ_ρ^2 scale as h_0^2 [12]. The number of pairs is limited by computational resources. Summing over all possible pairs, which is normally prohibitive computationally, returns the same result as a fully coherent search.

In principle, one should search over the unknowns $\cos\iota$ and ψ when computing ρ through Eq. (11). However, this adds to the already sizable computational burden occasioned by searching over pulsar spin parameters (see Sec. III B), when the number of SFT pairs is large. Accordingly, it is customary to average over $\cos\iota$ and ψ when computing $\tilde{\mathcal{G}}_{IJ}$, assuming uniform priors on both variables. The result is

$$\langle \tilde{\mathcal{G}}_{IJ} \rangle_{\cos\iota,\psi} = \frac{1}{10} \exp(-i\Delta\Phi_{\mathrm{IJ}}) \exp\{-i\pi\Delta T[\nu(T_I) - \nu(T_J)]\}(a_I a_J + b_I b_J), \tag{16}$$

with $a_I = a(T_I;\mathbf{n})$ and $b_I = b(T_I;\mathbf{n})$. One then computes the detection statistic ρ_{av} by replacing $\tilde{\mathcal{G}}_{IJ}^*$ by $\langle \tilde{\mathcal{G}}_{IJ}^* \rangle$ in Eq. (12). Similarly, the mean and variance of ρ_{av} can be computed by replacing $\tilde{\mathcal{G}}_{IJ}$ by $\langle \tilde{\mathcal{G}}_{IJ} \rangle$ in Eqs. (14) and (15). Note, importantly, that ρ_{av} is not equal to $\langle \rho \rangle_{\cos\iota,\psi}$ because $\mathcal{Y}_{IJ}$ depends implicitly on $\cos\iota$ and ψ if $h_0 \neq 0$. Once a first-pass search with ρ_{av} is complete, a follow-up search on any promising candidates can be performed, which searches explicitly over $\cos\iota$ and ψ to achieve maximum sensitivity. Tests in Sec. IV C illustrate that the detection statistic resulting from Eq. (16) is approximately 10%–15% lower (up to 47% lower in rare cases) than if the exact $\cos\iota$ and ψ values are used.

B. Astrophysical phase model

The cross-correlation algorithm in Sec. III A must be accompanied by a parametrized model for the phase and frequency of the signal as functions of time, in terms of which we express the factors $\Delta\Phi_{IJ}$ and $\nu(T_I) - \nu(T_J)$ in Eqs. (5) and (16). A target like SNR 1987A raises special challenges in this regard. It is young and spins down rapidly, accumulating phase by an amount k proportional to $\nu^{(k)} T_{\mathrm{obs}}^{k+1} \approx \nu T_{\mathrm{obs}} (\xi T_{\mathrm{obs}}/T_{\mathrm{age}})$ from the kth term of the Taylor expansion of the phase evolution after an observation time T_{obs}. One therefore needs approximately $N_{\mathrm{total}} \propto \xi^{10} T_{\mathrm{obs}}^{10} T_{\mathrm{lag}}^5$ templates to keep the overall phase error below $\pi/4$ with SFT time separation $T_{\mathrm{lag}} = 1$ hr [8] by tracking terms up to and including $\nu^{(4)}$. As noted in Sec. II B, N_{total} is suppressed strongly by the factor ξ^{10}, with $\xi^{10} \ll 1$ for SNR 1987A.

In the special but astrophysically plausible situation where the braking index $n = \nu\ddot{\nu}/\dot{\nu}^2$ changes slowly with time, one can take advantage of an alternative model for the gravitational-wave phase introduced in Chung *et al.* [8], stated in terms of astrophysical parameters (i.e., the magnetic field strength and the neutron star ellipticity) instead of spin-frequency derivatives. The model tracks the phase by assuming that the spin-down torque is the direct sum of gravitational-wave and electromagnetic components to a good approximation, with

$$\dot{\nu} = -\frac{32\pi^4 G \epsilon^2 I \nu^5}{5c^5} - \frac{2\pi^3 R_\star^6 B^2 \nu^{n_{\mathrm{em}}}}{3\mu_0 I c^3} \left(\frac{\pi R_\star}{c}\right)^{n_{\mathrm{em}}-3} \tag{17}$$

$$= -Q_1' \nu^5 - Q_2' \nu^{n_{\mathrm{em}}}. \tag{18}$$

In Eq. (18), $R_\star$ is the neutron star radius, B is the polar magnetic field, and n_{em} is the electromagnetic braking index. If the electromagnetic torque is proportional to a power of ν, then ν must enter the torque in the combination $R_\star \nu/c$ (i.e., the ratio of $R_\star$ to the characteristic lever arm, the light cylinder distance, $c/2\pi\nu$), on dimensional grounds. Hence, in terms of an arbitrary reference frequency ν_{ref}, we write $\dot{\nu} = -Q_1(\nu/\nu_{\mathrm{ref}})^5 - Q_2(\nu/\nu_{\mathrm{ref}})^{n_{\mathrm{em}}}$, with $Q_1 = Q_1' \nu_{\mathrm{ref}}^5$ and $Q_2 = Q_2' \nu_{\mathrm{ref}}^{n_{\mathrm{em}}}$. Throughout this paper, we set $\nu_{\mathrm{ref}} = 1$ Hz without loss of generality.

The spin-down model (18) tracks the phase in terms of four parameters: ν_0, Q_1', Q_2', and n_{em}. Theoretically, one expects $n_{\mathrm{em}} = 3$ for a magnetic dipole in vacuo [62]; however, observations of radio pulsars find $1.8 \leq n_{\mathrm{em}} < 3.0$ [63], and there exist several theoretical mechanisms consistent with $n_{\mathrm{em}} < 3$ [53,61,66]. If n_{em} is truly constant, then phase tracking requires $N_{\mathrm{total}} \propto \xi^6 T_{\mathrm{obs}}^3 T_{\mathrm{lag}}^3$ templates [8], and the search problem simplifies considerably. However, observations returning $n_{\mathrm{em}} \neq 3$ raise the specter of n_{em} evolving as the star spins down; indeed, the extended dipole braking model predicts $n_{\mathrm{em}} \to 3$ as $t \to \infty$ [61]. If n_{em} evolves too rapidly, it negates the advantage of Eq. (18) relative to a Taylor expansion $\{\nu, \dot{\nu}, \ddot{\nu}, \cdots\}$. This issue is quantified in Sec. IV D 3, and the parameter range where Eq. (18) remains useful is determined.

C. Numerical algorithm

The cross-correlation algorithm is implemented as part of the LIGO data analysis software suite (LAL[2] and

[2]https://www.lsc-group.phys.uwm.edu/dawsg/projects/lal.html

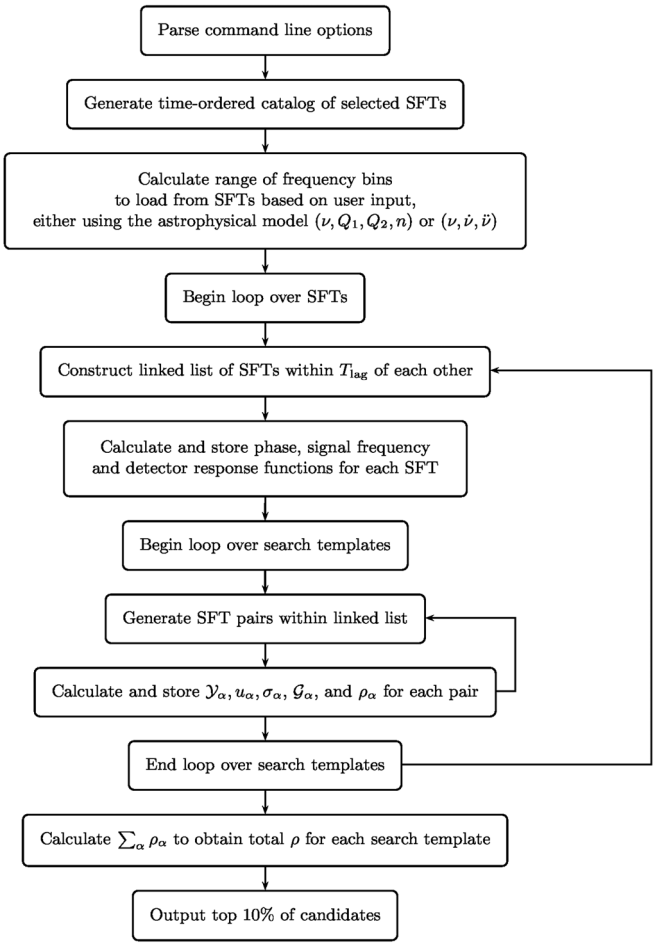

FIG. 2. Flowchart summarizing the cross-correlation algorithm used in the LALApps utility. Note that α labels the SFT index pair (I, J).

LALApps[3]) in a general-purpose form. First, the user can choose to search over the gravitational-wave frequency at the start of the observation, denoted by ν_0, and up to two frequency derivatives in the Taylor expansion of the phase model $(\nu_0, \dot{\nu}, \ddot{\nu})$, or use the astrophysical model described in Chung *et al.* [8] to search over ν_0, Q_1, Q_2, and n_{em}. Second, one can choose to target a single sky coordinate or search within a grid of sky coordinates. Third, the user can choose to run the search using a particular value for the inclination and polarization angles (ι and ψ) or average over these variables. Finally, the user can decide to pair up SFTs from only the same interferometer, different interferometers, or a combination.

The flow chart in Fig. 2 summarizes the numerical algorithm. First, the command-line options are parsed, and the relevant SFTs are located and read into a time-ordered catalog. Only the frequency bins corresponding to the user-specified search frequency range are extracted from the SFTs. Each SFT is paired with another which satisfies the user-specified selection criteria, e.g., the maximum time lag T_{lag}. For each unique SFT pair, the code loops over each search template and calculates the corresponding normalized cross-correlation statistic ρ for each template.

An important issue encountered in the implementation is the heavy use of central processing unit (CPU) virtual memory. When pairing up an entire year's worth of SFTs ($\sim 10^5$ SFTs ~ 1 Terabyte), it is not feasible to load and store all the SFTs in virtual memory while looping over the search templates. Instead, we construct a time-ordered linked list, which contains only SFTs within a sliding window of length T_{lag}, i.e., a first-in-first-out queue. The signal phase, frequency, and detector response functions are calculated at each T_I. Then SFT pairs are constructed within the sliding window, and we loop over the search templates. For each pair, we calculate and store the quantities $\mathcal{Y}_\alpha$, u_α, σ_α, $\mathcal{G}_\alpha$, and $\rho_\alpha = \sum_\alpha (u_\alpha \mathcal{Y}_\alpha + u_\alpha^* \mathcal{Y}_\alpha^*)$, which are defined in Ref. [12] and Sec. III A; to simplify notation, we use the subscript α to denote the index pair (I, J) [12]. As the window slides forward, we delete the SFT at the head of the linked list, add the next SFTs to its tail (as long as it satisfies the user-specified multiplication condition), and repeat the process. Once the loop over all possible pairs is finished, the final value of the detection statistic $\rho = \sum_\alpha \rho_\alpha$ for a particular search template is calculated. Finally, we output ρ (normalized by its standard deviation) along with the relevant search parameters used. Typically, we search up to $\sim 10^9$ templates and filter the output so that, e.g., only the highest 10% of ρ values are saved.

IV. ALGORITHM VERIFICATION

A. Distribution of ρ/σ_ρ when searching over pure noise

A basic consistency check is to run the search on simulated noise with no injected signal. The detector noise time series $n(t)$ is typically assumed to be Gaussian with zero mean. In this situation, according to Eq. (3), $\mathcal{Y}_\alpha$ is related to the noise power spectra in the SFTs centered at T_I and T_J. Hence, ρ_α is a product of two independent Gaussian variables with zero mean. Its probability density function (PDF) is a modified Bessel function of the second kind of order zero, with zero mean and finite variance [12]. Applying the central limit theorem, the sum of a large number of such zero-mean variables tends to a Gaussian random variable [67], as the number of SFT pairs, N_{pairs}, increases.

The mean μ_ρ and variance σ_ρ^2 of ρ in the low-signal limit are given by [12]

$$\mu_\rho = h_0^2 \sum_\alpha (u_\alpha \mathcal{G}_\alpha + u_\alpha^* \mathcal{G}_\alpha^*), \tag{19}$$

$$\sigma_\rho^2 = 2 \sum_\alpha |u_\alpha|^2 \sigma_\alpha^2, \tag{20}$$

where h_0 vanishes for pure noise, and u_α, $\mathcal{G}_\alpha$, and σ_α are defined in Eqs. (12), (5), and (13), respectively. We note

[3]https://www.lsc-group.phys.uwm.edu/dawsg/projects/lalapps.html

that these equations exclude self-correlations (i.e., pairing a SFT with itself), and Eq. (20) assumes $h_0 \ll |n(t)|$. We discuss how to generalize beyond the small-signal limit in Sec. IV B. The code outputs the normalized cross-correlation statistic ρ/σ_ρ, whose PDF should have zero mean and unit variance for pure noise. We emphasize that the mean μ and variance σ^2 of the PDF of ρ/σ_ρ should not be confused with the mean and variance of the prenormalized ρ distribution, given by Eqs. (19) and (20).

The simulated Gaussian noise is generated using the standard LALApps utility. This utility creates SFTs for user-specified values of signal strength h_0, single-sided power spectral density $[S_n(\nu)]^{1/2}$, SFT length T_{SFT}, total observation time T_{obs}, and signal parameters $\nu(t)$, α, δ, $\cos\iota$, and ψ. In order to vary N_{pairs} for testing purposes, we generate separate sets of 30-min SFTs for five different values of T_{obs} ranging from 1 hr (2 SFTs per interferometer) to 1 yr (17532 SFTs per interferometer) with zero signal strength ($h_0 = 0$) and random signal parameters. The standard analytic approximation of the single-sided power spectral density as a function of the signal frequency is [68]

$$S_n(\nu)^{1/2} \approx \alpha_0 \left[\alpha_1 \left(\frac{\nu}{150\ \mathrm{Hz}} \right)^{-56} + \alpha_2 \left(\frac{\nu}{150\ \mathrm{Hz}} \right)^{-4.52} + \alpha_3 \left(\frac{\nu}{150\ \mathrm{Hz}} \right)^{2} + \alpha_4 \right]^{1/2}, \tag{21}$$

with $\alpha_0 = (9 \times 10^{-46})^{1/2}\ \mathrm{Hz}^{-1/2}$, $\alpha_1 = 4.49$, $\alpha_2 = 0.16$, $\alpha_3 = 0.32$, and $\alpha_4 = 0.52$. In real LIGO data, variable phenomena like seismic noise make $S_n(\nu)$ time dependent on time scales of hours to days. Simulated noise does not suffer from this problem. SFTs are simulated for only two interferometers (H1 and L1), and the SFTs for each interferometer span identical times.

For each set of SFTs, we run the search using a frequency band of 10^{-2} Hz and a frequency resolution of 10^{-4} Hz, corresponding to 100 search templates for each pair (T_{lag}, T_{obs}). We consider five values of T_{obs} (1 hr $\leq T_{\mathrm{obs}} \leq$ 1 yr) and two values of T_{lag} for each T_{obs}, viz. 0 s and 3600 s. Setting $T_{\mathrm{lag}} = 0$ correlates only SFTs from different interferometers. This ensures that all pairs, and the resulting ρ_α values, are completely independent. For $T_{\mathrm{lag}} = 3600$ s, each SFT is paired with three others if we include data from two interferometers, and five others if we include data from three interferometers. In this case, the same SFT contributes to more than one ρ_α. As a result, the ρ_α values are not statistically independent. Coyne *et al.* [69] discussed the correction to ρ for dependent ρ_α, finding that ρ is distributed as a χ^2 distribution with 2 degrees of freedom instead of a Gaussian distribution (for more details, see Ref. [69]). This correction is crucial to an intermediate-duration search ($T_{\mathrm{obs}} \lesssim 10^4$ s). In this paper, we carry out a long-duration search ($T_{\mathrm{obs}} = 1$ yr). To test the above effect, we compare the PDFs of ρ for $T_{\mathrm{lag}} = 0$ (ρ_α independent) and $T_{\mathrm{lag}} = 3600$ s (ρ_α dependent) for T_{obs} in the range 1 hr $\leq T_{\mathrm{obs}} \leq$ 1 yr. The full results are presented below in Table I and Fig. 3. In brief, they confirm that the correction in Ref. [69] is appreciable for $T_{\mathrm{obs}} \lesssim 1$ day but negligible for $T_{\mathrm{obs}} = 1$ yr. The experiment is repeated 1000 times for each pair (T_{lag}, T_{obs}) with 100 templates, and the statistics of the resulting 10^5 ρ/σ_ρ values are compiled.

TABLE I. Mean μ and standard deviation σ of 10^5 values of the normalized cross-correlation statistic ρ/σ_ρ for a search over simulated Gaussian noise for observation times satisfying 1 hr $\leq T_{\mathrm{obs}} \leq$ 1 yr. For each value of T_{obs}, the number of SFT pairs, N_{pairs}, is listed, along with the maximum SFT pair separation T_{lag}.

T_{obs}	N_{pairs}	T_{lag} (s)	μ	σ
1 hour	2	0	−0.003393	1.035 527
	6	3600	0.001 966	1.033 288
5 hours	10	0	0.005 309	1.037 305
	46	3600	−0.002081	1.044 258
1 day	48	0	0.000 937	1.040 644
	236	3600	0.002 111	1.044 826
1 month	1440	0	0.000 613	1.042 374
	7196	3600	0.000 095	1.039 875
1 year	17 532	0	−0.004183	1.040 686
	87 656	3600	0.003 961	1.047 173

The mean μ and standard deviation σ of the ρ/σ_ρ PDFs are presented in Table I. The values of μ lie within the 95% confidence limits[4] and deviate from zero by at most 0.0053. The values of σ, however, are systematically ∼4% larger than unity and appear to increase with T_{obs}. The reason for this discrepancy is unclear. We keep this issue in mind as the analysis proceeds. Discrepancies at the $\lesssim$5% level are not expected to impact the search results significantly.

Figure 3 displays PDFs of ρ/σ_ρ (solid curves) for the trials listed in Table I. From top to bottom, the panels show ρ/σ_ρ for T_{obs} running from 1 hr to 1 yr for $T_{\mathrm{lag}} = 0$ s (left panel) and $T_{\mathrm{lag}} = 3600$ s (right panel). By way of comparison, Gaussian PDFs with zero mean and unit standard deviation are overplotted as dashed curves in each panel. The PDFs for $T_{\mathrm{obs}} = 1$ hr are clearly non-Gaussian. For $T_{\mathrm{lag}} = 0$ s (top row, left panel), the distribution is symmetric about zero but more sharply peaked than a Gaussian. For $T_{\mathrm{lag}} = 3600$ s (top row, right panel), the distribution peaks more sharply than a Gaussian and is significantly skewed. As T_{obs} increases, the PDFs for both T_{lag} values approach a Gaussian. For $T_{\mathrm{obs}} = 1$ month (fourth row in Fig. 3), the difference is nearly imperceptible by eye.

We quantify the Gaussianity of the PDFs in Fig. 3 by plotting their skewness and kurtosis excess in Fig. 4

[4]The 95% confidence limits for μ are $\pm 1.96\sigma N_{\mathrm{trial}}^{-1/2} \approx \pm 0.0064$, where N_{trial} is the number of trials (10^5).

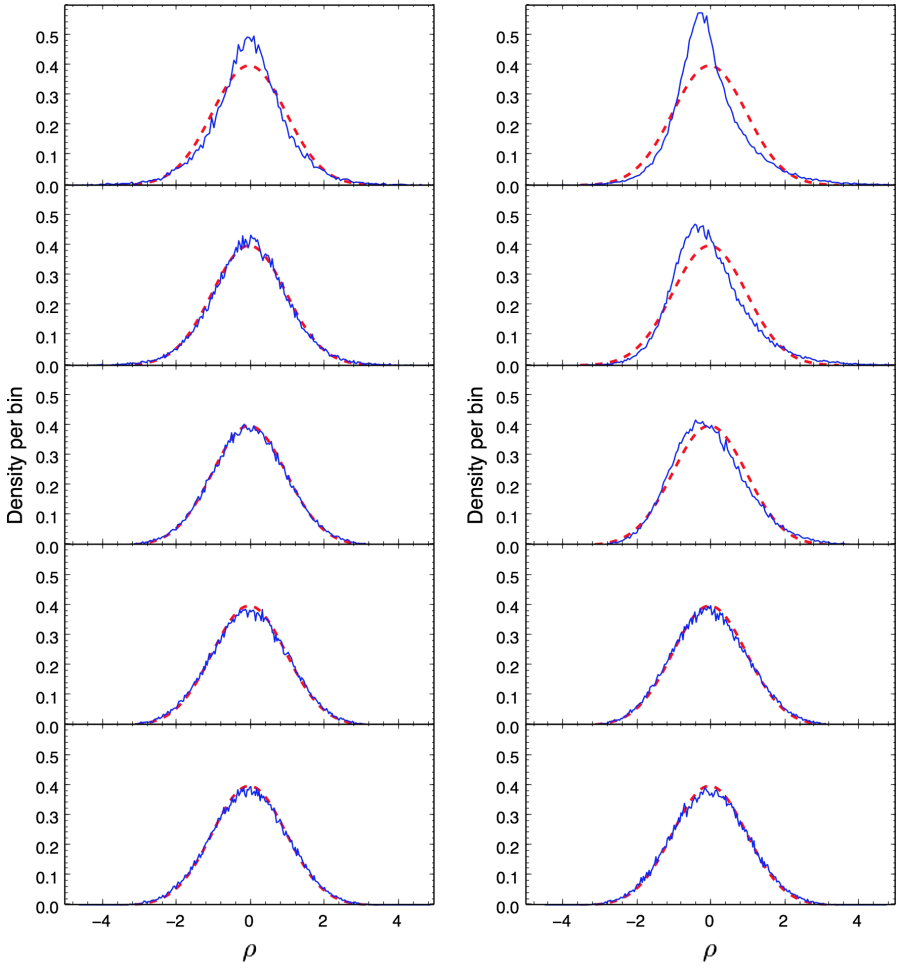

FIG. 3. PDFs of ρ/σ_ρ (solid curves) for $T_{\rm lag} = 0$ s (left) and $T_{\rm lag} = 3600$ s (right) for $T_{\rm obs} = 1$ hr, 5 hr, 1 day, 1 month, and 1 yr (top to bottom). For reference, the dashed curve shows a Gaussian with zero mean and unit variance.

as functions of $T_{\rm obs}$. The skewness of a distribution, which measures its reflection asymmetry, is defined as $\gamma_1 = \mu_3/\mu_2^{3/2}$, where μ_2 and μ_3 are the second and third central moments. For a Gaussian, γ_1 is zero. The kurtosis measures the peakiness and is defined as $\gamma_2 = \mu_4/\mu_2^2$, where μ_4 is the fourth central moment. For a Gaussian, one has $\gamma_2 = 3$. The kurtosis excess, $g_2 = \gamma_2 - 3$, therefore equals zero for a Gaussian. Figure 4 displays γ_1 and g_2 as functions of $\log(T_{\rm obs})$ for $T_{\rm lag} = 0$ s (left) and $T_{\rm lag} = 3600$ s (right). Error bars of size $\pm 2s_s$ and $\pm 2s_k$ are overplotted, where $2s_s = 2\sqrt{6/N_{\rm trial}} = 0.0155$ is twice the standard error of skewness, $2s_k = 2\sqrt{24/N_{\rm trial}} = 0.031$ is twice the standard error of kurtosis, and $N_{\rm trial} = 10^5$ is the total number of trials [70]. For $T_{\rm lag} = 3600$ s, the skewness and kurtosis decrease from $\gamma_1 = 1.03$, $g_2 = 4.09$ for $T_{\rm obs} = 1$ hr to $\gamma_1 = 0.0277$, $g_2 = 0.0006$ for $T_{\rm obs} = 1$ yr. For $T_{\rm lag} = 0$ s, when there is no overlap between SFT pairs and all ρ_α values are independent, the kurtosis also decreases as $T_{\rm obs}$ increases, from $g_2 = 2.204$ for $T_{\rm obs} = 1$ hr to $g_2 = 0.014$ for $T_{\rm obs} = 1$ yr. However, the skewness remains roughly centered at zero, fluctuating between $\gamma_1 = -0.010$ (for $T_{\rm obs} = 1$ hr) and $\gamma_1 = 0.015$ (for $T_{\rm obs} = 1$ day), which is within the standard errors. The shape of the ρ/σ_ρ PDF is therefore significantly affected by $T_{\rm obs}$ and, to a lesser extent, $T_{\rm lag}$. However, for $T_{\rm obs} \geq 1$ yr, the PDFs for $T_{\rm lag} = 0$ s and $T_{\rm lag} = 3600$ s agree with theoretical predications to an accuracy of better than 95% in μ, σ, γ_1, and g_2. The above results show that for intermediate-duration searches with $T_{\rm obs} \lesssim 10^4$ s (i.e., $T_{\rm obs} = 1$ hr, 5 hr in our test), the skewness and kurtosis deviate significantly from the expected values in a Gaussian distribution, and hence the correction to ρ discussed in Ref. [69] is required. However, in a long-duration search with $T_{\rm obs} = 1$ yr, the above moments of ρ match those of a Gaussian distribution to an accuracy above 95%, so the correction is negligible for the search in this paper.

B. Distribution of ρ/σ_ρ as a function of signal strength

The introduction of a gravitational-wave signal changes the distribution of ρ and ρ/σ_ρ. Most notably, the mean and variance increase with the signal strength. In Appendix A of Dhurandhar *et al.* [12], the statistics of the ρ distribution

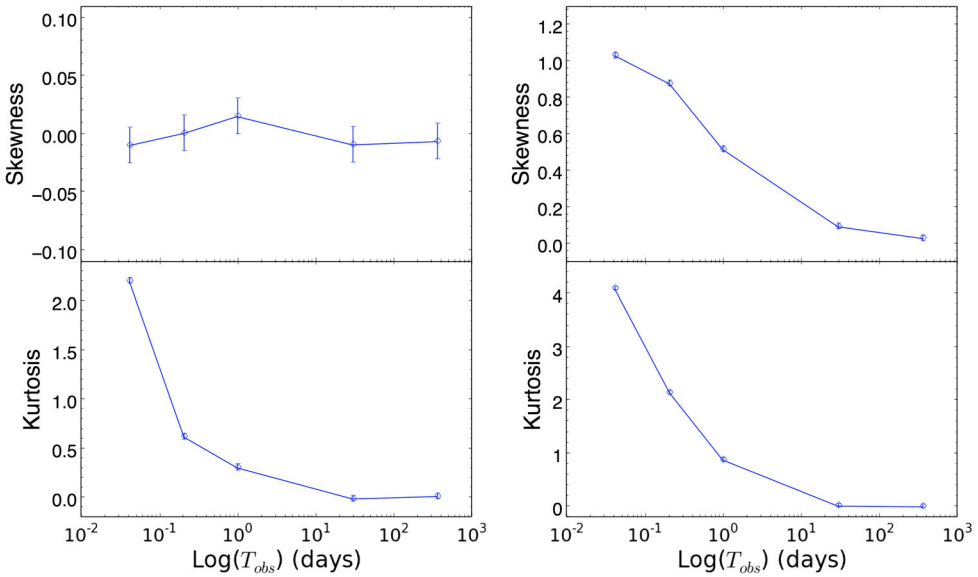

FIG. 4. Skewness γ_1 (top panels) and kurtosis excess $\gamma_2 - 3$ (bottom panels) of ρ/σ_ρ as functions of $T_{\rm obs}$, for $T_{\rm lag} = 0$ s (left) and $T_{\rm lag} = 3600$ s (right) when SFTs contain only Gaussian noise. The error bars (small vertical lines overplotted on the points) have peak-to-peak amplitudes of twice the standard error of skewness (top panels) and twice the standard error of kurtosis (bottom panels) (see text for definition).

are recalculated, including self-correlations and $\mathcal{O}(h_0^2)$ terms which are left out in the main body of their analysis. In the absence of self-correlations, which we neglect in this paper, one obtains

$$\mu_\rho = h_0^2 \sum_{IJ} (u_{IJ}\tilde{\mathcal{G}}_{IJ} + u_{IJ}^*\tilde{\mathcal{G}}_{IJ}^*), \tag{22}$$

$$\sigma_\rho^2 = 2\sum_{IJ}|u_{IJ}|^2\sigma_{IJ}^2 + \frac{h_0^2}{\Delta T}\sum_{I\neq J}|u_{IJ}|^2[\tilde{\mathcal{G}}_{II}S_n^{(J)} + \tilde{\mathcal{G}}_{JJ}S_n^{(I)}] + \mathcal{O}(h_0^4), \tag{23}$$

for the mean and variance of ρ, respectively. For the normalized statistic ρ/σ_ρ, whose noise-only PDF is a Gaussian with zero mean and unit variance, the mean and variance in the presence of a signal are given by

$$\mu = 2^{1/2}h_0^2\sum_\alpha |u_\alpha|, \tag{24}$$

$$\sigma^2 = \sum_{I\neq J}|u_{IJ}|^2\left[\frac{S_n^I S_n^J}{4\Delta T^2} + \frac{h_0^2}{2\Delta T}(\tilde{\mathcal{G}}_{II}S_n^J + \tilde{\mathcal{G}}_{JJ}S_n^I)\right] + \mathcal{O}(h_0^4), \tag{25}$$

respectively, where S_n^I is the single-sided power spectral density squared for the SFT centered at $t = T_I$. Self-correlation terms are not included in Eqs. (24) and (25). Again, we stress that μ and σ in Eqs. (24) and (25) are not derived from Eqs. (22) and (23) simply by dividing the latter equations by σ_ρ and σ_ρ^2, respectively. The PDF of ρ/σ_ρ is not truly Gaussian for pure noise, if dependent pairs are included [69]. However, the results in Sec. IV A demonstrate that the impact is negligible (i.e., the moments match those of a Gaussian distribution to an accuracy above 95%) for $T_{\rm obs} = 1$ yr, so we do not correct for this effect in this paper, as discussed in Sec. IV A.

We test Eqs. (24) and (25) against numerical results by injecting signals into simulated Gaussian noise with wave strains in the range $1\times10^{-26} \le h_0 \le 7.5\times10^{-23}$ at 150.1 Hz and zero spin-down. The h_0 range covers the regimes $h_0 \ll |n(t)|$, $h_0 < |n(t)|$, and $h_0 \gtrsim |n(t)|$. Again, we use the LALApps utility to generate 10^3 SFTs for each h_0 value, with arbitrary signal parameters $\alpha, \delta, \cos\iota$, and ψ. We take $T_{\rm obs} = 1$ yr, $T_{\rm lag} = 3600$ s, and search over a 0.01-Hz band centered on the signal frequency with a frequency resolution of 10^{-4} Hz. We only search the chosen α, δ, $\cos\iota$, and ψ values of the injected signal. From the theory, ρ/σ_ρ is maximized at the injected frequency value, which is 150.1 Hz in this case, and this maximum value appears to be dominant if the signal is strong enough. For verification purposes, we extract the 10^3 ρ/σ_ρ values at 150.1 Hz for each h_0 value tested. The mean and standard deviation of the 10^3 ρ/σ_ρ values are calculated and shown in Fig. 5.

The top panel of Fig. 5 plots μ as a function of h_0. For $h_0 \le 8\times10^{-26}$, μ gets very close to zero, which is as expected in the low signal limit. Above $h_0 = 8\times10^{-26}$, μ increases from ≈ 0.8 at $h_0 = 1\times10^{-25}$ to $\approx 3\times10^5$ at 7.5×10^{-23}, growing $\propto h_0^2$ as expected from Eq. (24).

The bottom panel of Fig. 5 shows σ as a function of h_0. One can distinguish three regimes. For $h_0 \le 1\times10^{-25}$, i.e., $h_0 \ll |n(t)|$, the signal is too small to be detectable, giving the same unit standard deviation as the results obtained in Sec. IV A for pure noise. In the intermediate regime $1\times10^{-25} \le h_0 \le 2\times10^{-25}$ between the vertical dashed lines, where the signal is small but still detectable, σ grows

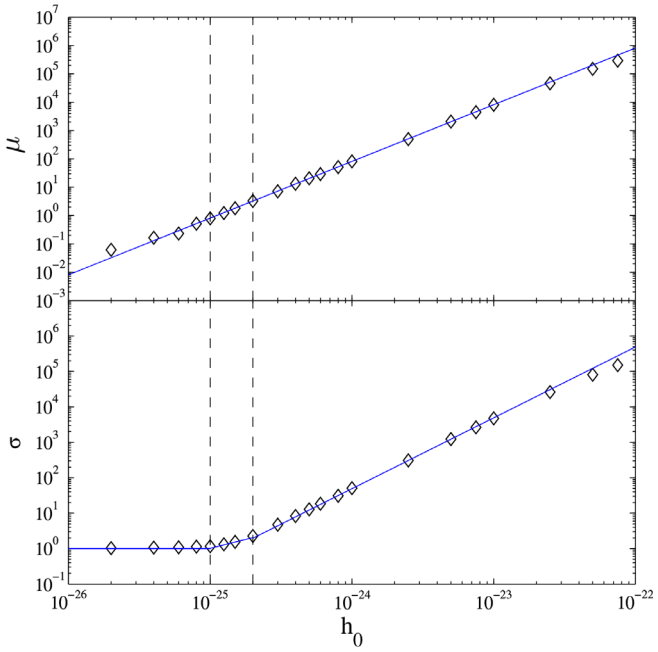

FIG. 5. The mean μ (top panel) and standard deviation σ (bottom panel) of the normalized cross-correlation statistic ρ/σ_ρ as a function of injected gravitational-wave strain h_0. The injected signals have arbitrary parameters α, δ, $\cos\iota$, and ψ, and a fixed frequency of 150.1 Hz with zero spin-down. Each point comes from 10^3 ρ/σ_ρ values for given h_0. The solid curves match the approximation predicted by Eqs. (24) and (25), and the vertical dashed lines mark the three h_0 regimes [$h_0 \ll |n(t)|$, $h_0 < |n(t)|$ and $h_0 \gtrsim |n(t)|$].

approximately $\propto h_0$ as predicted by Eq. (25), and the $\mathcal{O}(h_0^4)$ terms are negligible. As h_0 increases further, σ tends towards the scaling $\sigma \propto h_0^2$. Above $h_0 \approx 10^{-24}$, the $\mathcal{O}(h_0^4)$ terms in Eq. (25) are dominate. In practice, realistic astrophysical signals are unlikely to fall in the third regime. For an optimistic yet realistic signal strength satisfying $10^{-25} \lesssim h_0 \lesssim 10^{-24}$, μ and σ scale approximately as h_0^2, as predicted by Eqs. (24) and (25).

C. Averaging over $\cos\iota$ and ψ

The inclination and polarization angles, ι and ψ, which modulate the amplitude of a gravitational-wave signal, are not known for the compact object in SNR 1987A and should strictly be included in the set of search parameters. To economize computationally, however, it is often preferable to average over $\cos\iota$ and ψ in a first-pass search. If a suitable candidate is identified, follow-up searches can include these parameters, once the number of templates is narrowed down. In this subsection, we quantify the loss of sensitivity occasioned by the averaging process.

When averaging over $\cos\iota$ and ψ, the unaveraged signal cross-correlation function $\tilde{\mathcal{G}}_{IJ}$ in Eq. (5) is replaced by the averaged version [64]

$$\langle \tilde{\mathcal{G}}_{IJ} \rangle_{\psi,\cos\iota} = \frac{1}{4\pi} \int_0^{2\pi} d\psi \int_{-1}^{1} d(\cos\iota) \tilde{\mathcal{G}}_{IJ}. \quad (26)$$

The result is given by Eq. (16), applying the averaged versions of Eqs. (6)–(9) [12].

Let $\cos\iota_{\rm real}$ and $\psi_{\rm real}$ denote the $\cos\iota$ and ψ values of an injected signal, and let $\cos\iota_{\rm test}$ and $\psi_{\rm test}$ be the associated search variables in a mock search. We create 400 injections on a uniformly spaced 20×20 grid of $\cos\iota_{\rm real}$ and $\psi_{\rm real}$ values, using the LALApps utility as in Sec. IV A. Signals are injected into 1 year of 30-min SFTs (from H1 and L1) with $h_0/\sqrt{S_n(\nu)} = 9.635\ {\rm Hz}^{1/2}$ at frequency 991.413 Hz. Sky coordinates (α, δ) are chosen arbitrarily to be $(1.16357, -0.0439203)$. For each injection, we run two mock searches using the following: (1) $\tilde{\mathcal{G}}_{IJ}$, the exact signal parameters (α, δ), and a 10×10 grid of $\cos\iota_{\rm test}$ and $\psi_{\rm test}$ values, and (2) $\langle \tilde{\mathcal{G}}_{IJ} \rangle_{\cos\iota,\psi}$ and the exact signal parameters (α, δ). Both searches analyze the same SFTs across a frequency band of full width 0.003 Hz centered on the injected signal frequency, with a resolution of 10^{-5} Hz and $T_{\rm lag} = 3600$ s. We extract the maximum normalized statistics ρ/σ_ρ at the injected frequency. Among the 100 values of ρ/σ_ρ from the first set of searches, we denote the maximum, mean, and minimum values with $(\rho/\sigma_\rho)_{\rm max}$, $(\rho/\sigma_\rho)_{\rm mean}$, and $(\rho/\sigma_\rho)_{\rm min}$, respectively. From the second search, $(\rho/\sigma_\rho)_{\rm avg}$ denotes the single normalized statistic returned by using the averaged cross-correlation function $\langle \tilde{\mathcal{G}}_{IJ} \rangle_{\psi,\cos\iota}$. We emphasize that $(\rho/\sigma_\rho)_{\rm mean}$ and $(\rho/\sigma_\rho)_{\rm avg}$ are different quantities; the former involves $\tilde{\mathcal{G}}_{IJ}$, while the latter involves $\langle \tilde{\mathcal{G}}_{IJ} \rangle_{\psi,\cos\iota}$.

Figure 6 compares $(\rho/\sigma_\rho)_{\rm avg}$ to $(\rho/\sigma_\rho)_{\rm max}$ (left panel), $(\rho/\sigma_\rho)_{\rm mean}$ (middle panel), and $(\rho/\sigma_\rho)_{\rm min}$ (right panel). The relevant ratios are plotted as contours on the plane spanned by $\cos\iota_{\rm real}$ and $\psi_{\rm real}$. Note that $(\rho/\sigma_\rho)_{\rm avg}$ is plotted as the numerator in order to make the comparison straightforward. The left panel corresponds to trials where ($\cos\iota_{\rm test}$, $\psi_{\rm test}$) happens to be close to ($\cos\iota_{\rm real}$, $\psi_{\rm real}$), in which $(\rho/\sigma_\rho)_{\rm avg}$ is expected to be smaller than $(\rho/\sigma_\rho)_{\rm max}$. We find $0.534 \le (\rho/\sigma_\rho)_{\rm avg}/(\rho/\sigma_\rho)_{\rm max} \le 0.943$ for the 400 injections. These results are from the worst case using $\langle \tilde{\mathcal{G}}_{IJ} \rangle_{\cos\iota,\psi}$, yet the loss in sensitivity is tolerable. The middle panel plots the ratio of $(\rho/\sigma_\rho)_{\rm avg}$ to the mean value of ρ/σ_ρ among the 400 injections. The ratio fluctuates slightly between 1.035 and 1.118; using $\langle \tilde{\mathcal{G}}_{IJ} \rangle_{\cos\iota,\psi}$ typically sacrifices $\lesssim$10% sensitivity and can even improve it slightly for certain ($\cos\iota_{\rm test}$, $\psi_{\rm test}$) combinations. The right panel compares $(\rho/\sigma_\rho)_{\rm avg}$ with $(\rho/\sigma_\rho)_{\rm min}$, when ($\cos\iota_{\rm test}$, $\psi_{\rm test}$) is far from ($\cos\iota_{\rm real}$, $\psi_{\rm real}$). The ratio ranges between 1.33 and 2.802; i.e., there is a significant advantage in using $\langle \tilde{\mathcal{G}}_{IJ} \rangle_{\cos\iota,\psi}$. In every panel, the results appear to depend more on $\cos\iota$ than ψ, but, near $\cos\iota \approx 0.0$ where the signal is weakest, the variation with ψ is more apparent.

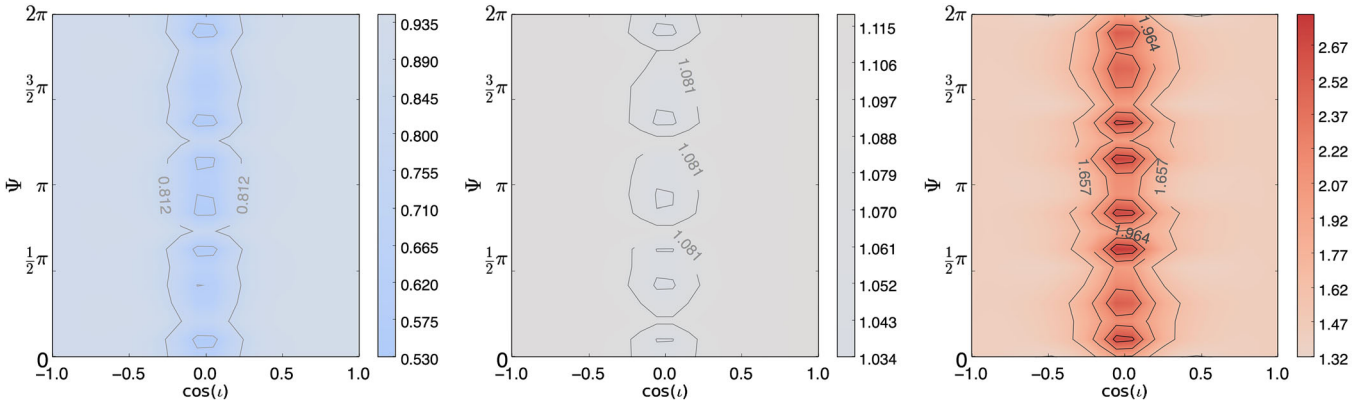

FIG. 6. Ratio of the normalized detection statistic $(\rho/\sigma_\rho)_{\text{avg}}$ computed with the averaged cross-correlation function $\langle\tilde{\mathcal{G}}_{IJ}\rangle_{\cos\iota,\psi}$ divided by the maximum, mean, and minimum values of the normalized detection statistic using the unaveraged $\tilde{\mathcal{G}}_{IJ}$ as a function of the injection angles $(\cos\iota_{\text{real}}, \psi_{\text{real}})$ (left, middle, and right panels, respectively). The averaged statistic $\langle\tilde{\mathcal{G}}_{IJ}\rangle_{\cos\iota,\psi}$ performs nearly as well as $\tilde{\mathcal{G}}_{IJ}$ for a fraction of the computational cost, sacrificing $\lesssim$50% sensitivity in the (rare) worst cases (left panel) and $\lesssim$10% sensitivity typically (middle panel). It yields better sensitivity in the best cases (right panel).

This matches expectations: $\tilde{\mathcal{G}}_{IJ}$ depends more strongly on $\cos\iota$ via $\mathcal{A}_+$ and $\mathcal{A}_\times$ in Eqs. (6) and (7) than on ψ via F_+ and $F_\times$ in Eqs. (8) and (9). When the inclination angle approaches 90 degrees (i.e., $\cos\iota \approx 0.0$), the gravitational-wave strain in Eq. (10) is smaller than for smaller inclination angles, and hence the sensitivity sacrificed by averaging $\tilde{\mathcal{G}}_{IJ}$ is more obvious when there is a weaker signal. In every panel, for $|\cos\iota| \lesssim 0.25$, the contours make periodic patterns along the vertical axis caused by variation of ψ with a period approximately equal to π, as expected from the periodic functions F_+ and $F_\times$ in Eqs. (8) and (9).

In summary, $\langle\tilde{\mathcal{G}}_{IJ}\rangle_{\cos\iota,\psi}$ performs nearly as well as $\tilde{\mathcal{G}}_{IJ}$ for a fraction of the computational cost, sacrificing $\lesssim$50% sensitivity in the (rare) worst cases and $\lesssim$10% sensitivity typically.

D. Astrophysical spin-down parameters

As described in Sec. III C, one can choose to search over the Taylor coefficients $(\nu_0, \dot{\nu}, \ddot{\nu})$ or the parameters $(\nu_0, Q_1, Q_2, n_{\text{em}})$ that define the astrophysical spin-down model described in Sec. III B. The latter approach performs better when n_{em} is constant, to a good approximation over the observation time. In this subsection, we quantify the relative performance of the two approaches and show that the relevant "observation time" is T_{lag} rather than T_{obs} because the cross-correlation algorithm is semicoherent. The computational cost of the search is analyzed in Chung *et al.* [8].

1. Astrophysical model versus Taylor expansion

We begin by running a single search for an injected signal that is spinning down using both the astrophysical model and Taylor expansion. We inject a signal into 30-min SFTs (from H1 and L1) for the 1-yr observation period with the parameters listed in Table II, which lie in the typical ranges discussed in Sec. II. Note that the utility LALApps was not written to accommodate a general spin-down model in the form (17) for generating synthetic data, so we input the frequency and its first three derivatives instead, as calculated from Eq. (17).

Two searches are carried out with this mock data set for $T_{\text{lag}} = 3600$ s. The first search uses the astrophysical model. The second uses the Taylor expansion. The search parameter ranges encompass the injected signal and are quoted in Table III. For now, we take $n_{\text{em}} = 3$ to be constant. The evolution of n_{em} is discussed in Sec. IV D 3.

Figure 7 presents the normalized detection statistic ρ/σ_ρ from the first search as a function of parameter pairs from the set $\{\nu_0, Q_1, Q_2\}$ in three separate contour plots. Similarly, Fig. 8 presents contours of ρ/σ_ρ as a function of parameter pairs from the set $\{\nu_0, \dot{\nu}, \ddot{\nu}\}$. The statistic peaks when the trial parameter values are closest to the injected values $(\nu_{0\text{signal}}, Q_{1\text{signal}}, Q_{2\text{signal}})$ or $(\nu_{0\text{signal}}, \dot{\nu}_{\text{signal}}, \ddot{\nu}_{\text{signal}})$ as expected. The first search generates a higher maximum $(\rho/\sigma_\rho \approx 2 \times 10^5)$ than the second $(\rho/\sigma_\rho \approx 1.3 \times 10^5)$

TABLE II. Injection parameters used to create the synthetic data analyzed in Sec. IV D 1. The frequency derivatives correspond to spin-down parameters $Q_{1\text{signal}} = 3.5 \times 10^{-19}$ Hz s^{-1} and $Q_{2\text{signal}} = 1 \times 10^{-17}$ Hz s^{-1} (i.e., $\epsilon = 4.52 \times 10^{-4}$ and $B = 4.05 \times 10^{11}$ G) according to Eqs. (17) and (18).

Injection parameter	Value	Units
$h_0/\sqrt{S_n(\nu)}$	3.33	Hz$^{1/2}$
$\nu_{0\text{signal}}$	150.1	Hz
$\dot{\nu}_{0_{\text{signal}}}$	-2.67×10^{-8}	Hz s^{-1}
$\ddot{\nu}_{0_{\text{signal}}}$	2.37×10^{-17}	Hz s^{-2}
$\dddot{\nu}_{0_{\text{signal}}}$	-3.80×10^{-26}	Hz s^{-3}

TABLE III. Search parameter ranges using the astrophysical model and the Taylor series. The ranges are centered on the injected signals. We take $n_{\mathrm{em}} = 3$ to be constant and discuss the evolution of n_{em} in Sec. IV D 3. The range width column defines the domain of the search parameter assuming that it is centered on the injection.

	Search parameter	Range width	Resolution	Units
Astrophysical model	ν_0	0.5	0.005	Hz
	Q_1	5×10^{-19}	0.05×10^{-19}	$\mathrm{Hz\,s^{-1}}$
	Q_2	2×10^{-17}	0.02×10^{-17}	$\mathrm{Hz\,s^{-1}}$
Taylor series	ν_0	0.5	0.005	Hz
	$\dot{\nu}_0$	2×10^{-8}	0.01×10^{-8}	$\mathrm{Hz\,s^{-1}}$
	$\ddot{\nu}_0$	2×10^{-17}	0.01×10^{-17}	$\mathrm{Hz\,s^{-2}}$

because only the first and second frequency derivatives are searched in the second test, whereas the first search tracks the phase exactly. The superiority of searching astrophysical parameters becomes more dominant when we inject a signal with a faster spin-down rate.

2. Including or excluding Q_1 and Q_2

One may doubt whether the astrophysical spin-down model is correct and wonder how the search can benefit from including spin-down parameters. We now test how much sensitivity is sacrificed by searching over ν_0 and

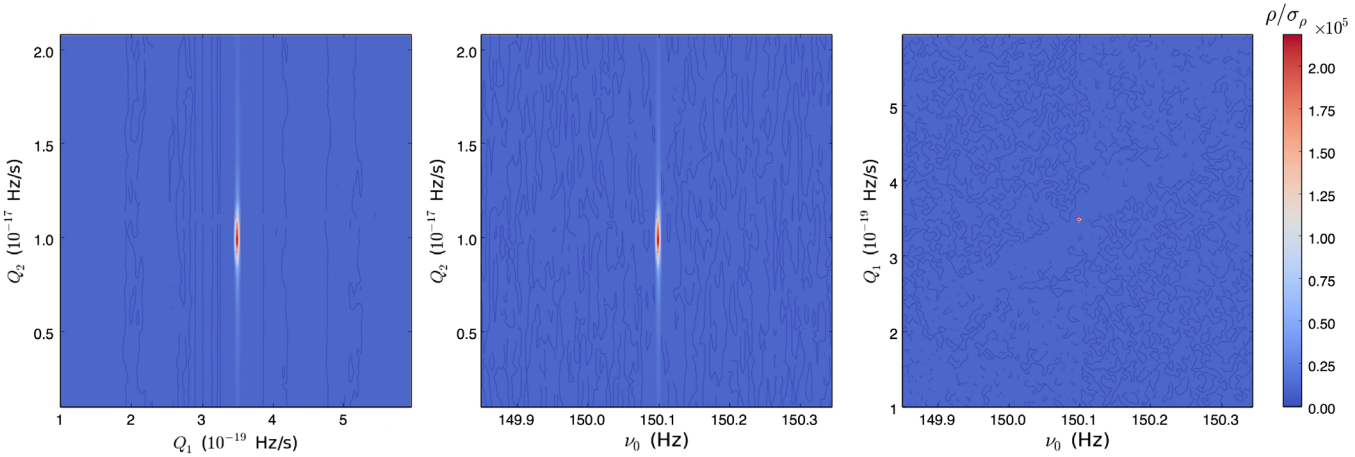

FIG. 7. Normalized detection statistic ρ/σ_ρ as a function of trial parameter value pairs from the set $\{\nu_0, Q_1, Q_2\}$. The injected values are $\nu_{0\mathrm{signal}} = 150.1$ Hz, $Q_{1\mathrm{signal}} = 3.5 \times 10^{-19}$ $\mathrm{Hz\,s^{-1}}$, $Q_{2\mathrm{signal}} = 1 \times 10^{-17}$ $\mathrm{Hz\,s^{-1}}$.

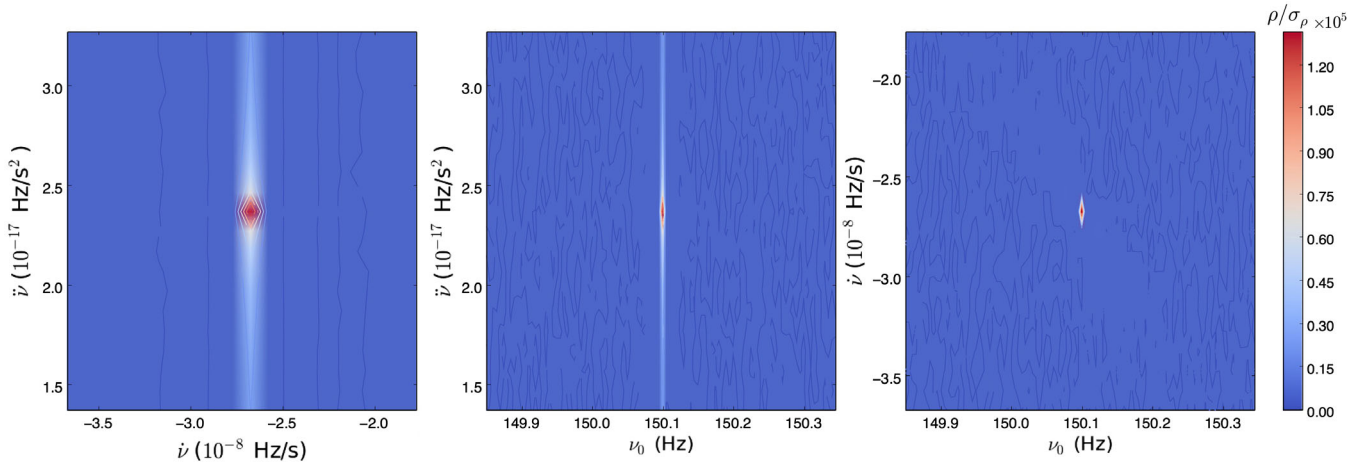

FIG. 8. Normalized detection statistic ρ/σ_ρ as a function of trial parameter value pairs from the set $\{\nu_0, \dot{\nu}, \ddot{\nu}\}$. The injected values are $\nu_{0\mathrm{signal}} = 150.1$ Hz, $\dot{\nu}_{0_{\mathrm{signal}}} = -2.67 \times 10^{-8}$ $\mathrm{Hz\,s^{-1}}$, $\ddot{\nu}_{0_{\mathrm{signal}}} = 2.37 \times 10^{-17}$ $\mathrm{Hz\,s^{-2}}$, $\dddot{\nu}_{0_{\mathrm{signal}}} = -3.80 \times 10^{-26}$ $\mathrm{Hz\,s^{-3}}$.

TABLE IV. Spin-down parameter ranges for the injected signals analyzed in Sec. IV D 2 in order to compare the results of searching ν_0 only and searching ν_0, Q_1, and Q_2. A grid of 15×17 values of $Q_{1\text{signal}}$ and $Q_{2\text{signal}}$, evenly spaced on a logarithmic scale, is chosen within the ranges. The corresponding ranges of the astrophysical parameters ϵ and B in Eq. (17) are also quoted.

Injection parameter	Astrophysical parameter
$1 \times 10^{-22} \leq Q_{1\text{signal}} \leq 1.64 \times 10^{-18}$ Hz s^{-1}	$7.65 \times 10^{-6} \leq \epsilon \leq 9.79 \times 10^{-4}$
$1 \times 10^{-21} \leq Q_{2\text{signal}} \leq 1 \times 10^{-13}$ Hz s^{-1}	4.05×10^{9} G $\leq B \leq 4.05 \times 10^{13}$ G

neglecting spin-down, as compared to searching a combination of (ν_0, Q_1, Q_2) according to the astrophysical spin-down model (17). Again, we assume n_{em} is constant for simplicity; cf. Sec. IV D 3. We inject signals with a range of wave strains h_0 but identical $\nu_0 = 150.1$ Hz. For a specific wave strain, a grid of 15×17 values of $Q_{1\text{signal}}$ and $Q_{2\text{signal}}$ is chosen within the ranges listed in Table IV. The signal parameters are astrophysically relevant, in line with the discussion in Sec. II, and they are affordable from the perspective of computing cost. Each signal, which is spinning down, is injected into 30-min SFTs (from H1 and L1) for a whole year. Two sets of searches, excluding and including Q_1 and Q_2 in the search parameters, are run over the parameter ranges in Table V with $T_{\text{lag}} = 3600$ s, targeted at the same injections. We analyze only the largest ρ/σ_ρ value returned.

Figure 9 displays the results from the first set of searches, where ν_0 is the only search parameter (i.e., $Q_1 = Q_2 = 0$). The top row displays the results for relatively strong signals $[h_0 = 1 \times 10^{-23},\ h_0/\sqrt{S_n(\nu)} = 0.33\ \text{Hz}^{1/2}]$ on the $Q_{1\text{signal}} - Q_{2\text{signal}}$ plane. The left panel shows that ρ/σ_ρ peaks at ~400 in the bottom-left corner of the plot and drops dramatically when $Q_{1\text{signal}} \geq 10^{-19}$ Hz s^{-1} and $Q_{2\text{signal}} \geq 10^{-16}$ Hz s^{-1}. In the right panel, the frequency at which ρ/σ_ρ peaks is lower than $\nu_{0\text{signal}} = 150.1$ Hz and decreases as $Q_{1\text{signal}}$ and $Q_{2\text{signal}}$ increase. We expect the latter discrepancy; we are searching for a constant-ν signal, while the injection is spinning down, and the discrepancy grows as $\dot{\nu}_{\text{signal}}$ increases. The middle row of Fig. 9 shows the same thing for weaker signals with $h_0 = 5 \times 10^{-24}$ and $h_0/\sqrt{S_n(\nu)} = 0.167\ \text{Hz}^{1/2}$. Here, ρ/σ_ρ peaks at ~100, and the frequency where it peaks decreases faster than in the previous case. In the bottom row, with $h_0 = 1 \times 10^{-24}$ and $h_0/\sqrt{S_n(\nu)} = 0.033\ \text{Hz}^{1/2}$, the signals are too weak to be detectable. Excluding spin-down therefore leads to significant loss in sensitivity, as compared to Sec. IV B.

Figure 10 displays the results from the second set of searches, where not only ν_0 but also Q_1 and Q_2 are searched. In the top row $[h_0 = 1 \times 10^{-23},\ h_0/\sqrt{S_n(\nu)} = 0.33\ \text{Hz}^{1/2}]$, ρ/σ_ρ is larger than in the top row of Fig. 9 (i.e., same h_0), reaching as high as $\sim 3.26 \times 10^3$ over a broad range of $Q_{1\text{signal}}$ and $Q_{2\text{signal}}$ ($Q_{1\text{signal}} \lesssim 4 \times 10^{-19}$ Hz s^{-1} and the whole range of $Q_{2\text{signal}}$ tested). In the right panel in the top row, the largest ρ/σ_ρ always occurs at the injected frequency $\nu_{0\text{signal}} = 150.1$ Hz. In the middle row $[h_0 = 1 \times 10^{-24},\ h_0/\sqrt{S_n(\nu)} = 0.033\ \text{Hz}^{1/2}]$, signals which are undetectable in Fig. 9 remain detectable in Fig. 10. Again, ρ/σ_ρ peaks at $\nu_{0\text{signal}} = 150.1$ Hz. In the bottom row $[h_0 = 3 \times 10^{-25},\ h_0/\sqrt{S_n(\nu)} = 0.01\ \text{Hz}^{1/2}]$, the signals become lost in the noise in both figures, close to the minimum detectable h_0 calculated in Sec. IV B.

In summary, we verify that as long as a spinning-down signal is strong enough or spins down slowly, it can be detected whether or not Q_1 and Q_2 are excluded from the search. However, when a signal is weak $[h_0 \lesssim 5 \times 10^{-24},\ h_0/\sqrt{S_n(\nu)} \lesssim 0.167\ \text{Hz}^{1/2}]$ or the frequency evolves quickly ($|\dot{\nu}| \gtrsim 1 \times 10^{-8}$ Hz s^{-1}), excluding Q_1 and Q_2 causes significant loss in sensitivity, enlarging the detectable h_0 threshold ~10 times.

3. Braking index evolution

The electromagnetic braking index n_{em} for radio pulsars is observed to satisfy $n_{\text{em}} < 3$ [63], in contrast with classical magnetic dipole braking ($n_{\text{em}} = 3$). This raises the possibility that n_{em} evolves, as the neutron star spins

TABLE V. Search parameter ranges for the synthetic signals with injection parameters quoted in Table IV. The upper half of the table refers to searching ν_0 only (i.e., $Q_1 = Q_2 = 0$). The lower half refers to searching ν_0, Q_1, and Q_2. The ranges encompass the injected signals.

	Search parameter	Range	Resolution	Units
Search ν_0 only	ν_0	135.45–150.15	0.01	Hz
Search ν_0, Q_1 and Q_2	ν_0	150.095–150.105	0.001	Hz
	Q_1	0.9–1.1	0.02	$Q_{1\text{signal}}$
	Q_2	0.9–1.1	0.02	$Q_{2\text{signal}}$

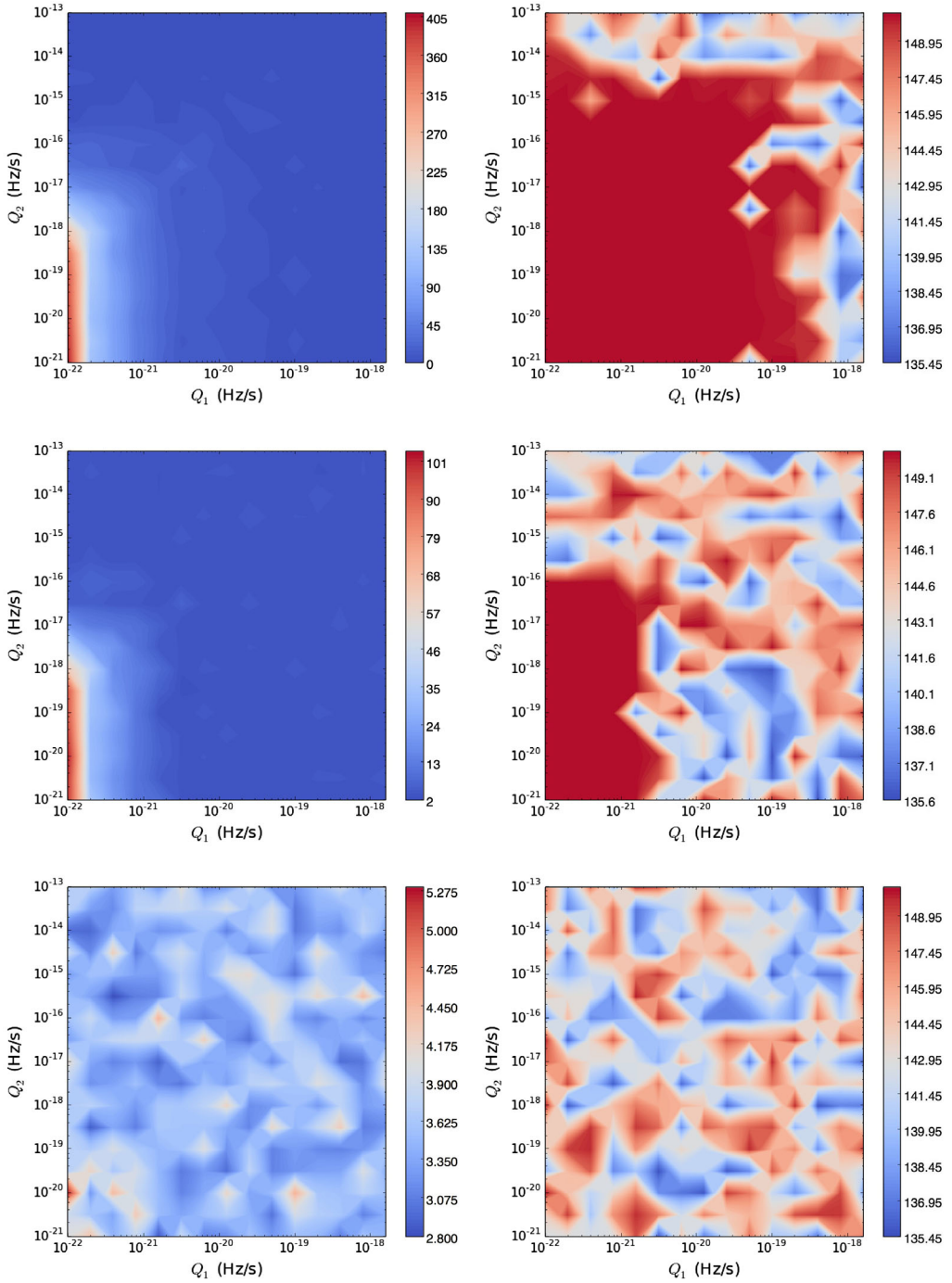

FIG. 9. Maximum ρ/σ_ρ returned as a function of $Q_{1\mathrm{signal}}$ and $Q_{2\mathrm{signal}}$ values when searching over ν_0 only (i.e., $Q_{1\mathrm{trial}} = Q_{2\mathrm{trial}} = 0$) (left), and the corresponding frequency at which ρ/σ_ρ peaks (right) for $h_0 = 1 \times 10^{-23}$ and $h_0/\sqrt{S_n(\nu)} = 0.33\ \mathrm{Hz}^{1/2}$ (top), $h_0 = 5 \times 10^{-24}$ and $h_0/\sqrt{S_n(\nu)} = 0.167\ \mathrm{Hz}^{1/2}$) (middle), and $h_0 = 1 \times 10^{-24}$ and $h_0/\sqrt{S_n(\nu)} = 0.033\ \mathrm{Hz}^{1/2}$ (bottom).

down, increasing N_{total} over and above the already heavy cost of searching over Q_1 and Q_2. We now quantify how much sensitivity is sacrificed by assuming n_{em} is constant.

Specifically, if we fix $n_{\mathrm{em}} = 3$ in the search, yet the true value is $n_{\mathrm{em}} = 3 - \Delta n_{\mathrm{em}}(t)$, we find that the sensitivity does not change significantly, as long as T_{lag} (the maximum interval over which the cross-correlation algorithm requires phase coherence) is smaller than $|\xi|^{-1} T_{\mathrm{age}}$. Instead, the signal is recovered with a similar signal-to-noise ratio but at a modified value of Q_2. The result holds if n_{em} is constant or evolves slowly on the time scale $|\xi|^{-1} T_{\mathrm{age}}$, with the signal location in Q_2 evolving on a similar time scale.

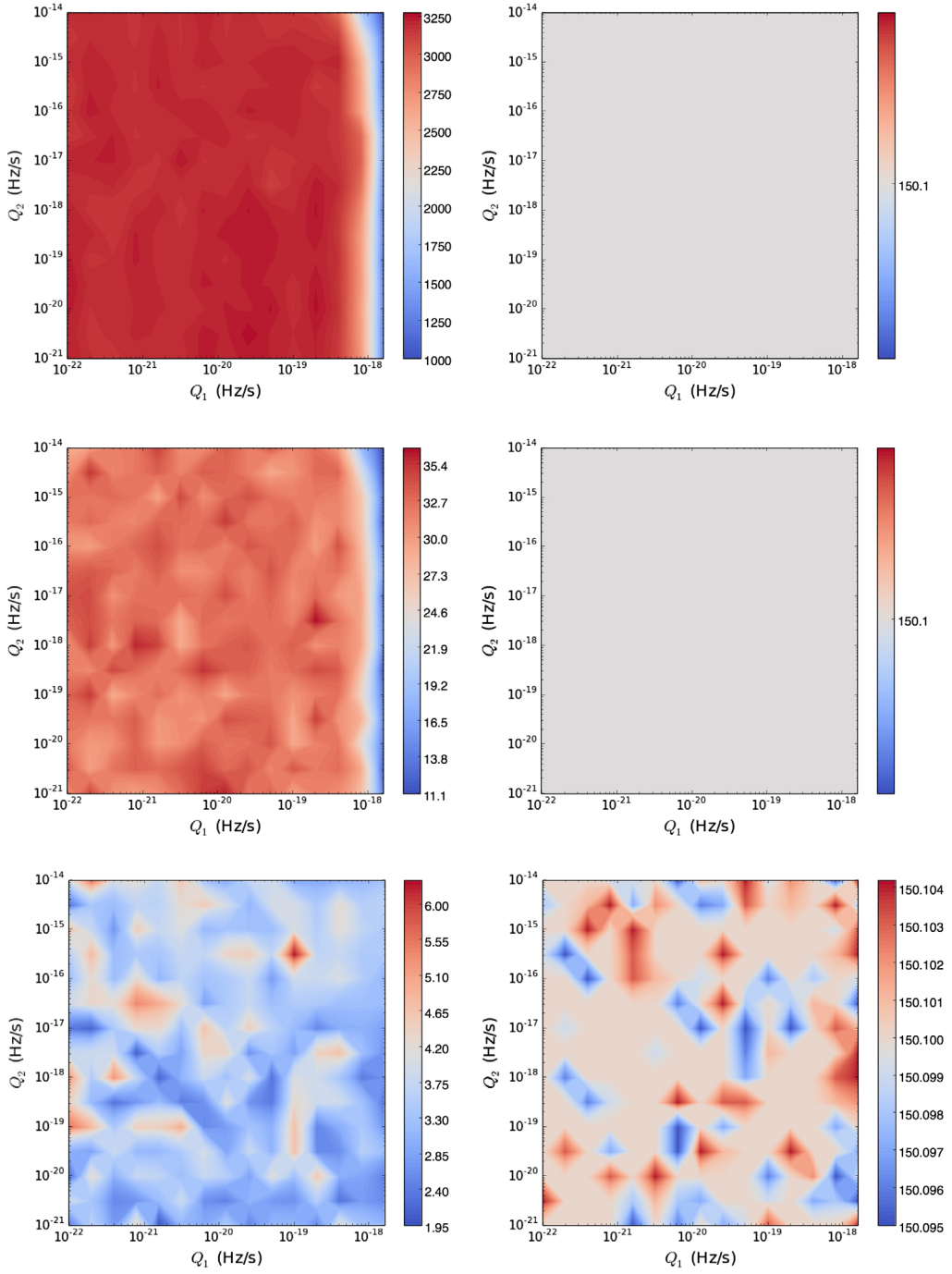

FIG. 10. Maximum ρ/σ_ρ returned as a function of $Q_{1\mathrm{signal}}$ and $Q_{2\mathrm{signal}}$ values when searching over ν_0, Q_1, and Q_2 (left), and the corresponding frequency at which ρ/σ_ρ peaks (right) for $h_0 = 1 \times 10^{-23}$ and $h_0/\sqrt{S_n(\nu)} = 0.33\ \mathrm{Hz}^{1/2}$ (top), $h_0 = 1 \times 10^{-24}$ and $h_0/\sqrt{S_n(\nu)} = 0.033\ \mathrm{Hz}^{1/2}$ (middle), and $h_0 = 3 \times 10^{-25}$ and $h_0/\sqrt{S_n(\nu)} = 0.01\ \mathrm{Hz}^{1/2}$ (bottom).

Figure 11 presents results from mock searches demonstrating the behavior above. We simulate spinning-down signals at three different wave strains whose parameters are quoted in Table VI, generating 1 year of 30-min SFTs (from H1 and L1). For each value of h_0, we inject signals with eight different values of n_{emsignal}. The search parameters are quoted in Table VII. The electromagnetic braking index $n_{\mathrm{em}} = 3$ is held fixed in every search. For each value of $h_{0\mathrm{signal}}$ and n_{emsignal}, the above test is repeated 100 times. We extract the maximum ρ/σ_ρ as well as the corresponding Q_2' value which maximizes ρ/σ_ρ from each of the 100 trials, and we plot the mean values of $(\rho/\sigma_\rho)_{\mathrm{max}}$ and Q_2' as functions of n_{emsignal} in Fig. 11. The variation in $(\rho/\sigma_\rho)_{\mathrm{max}}$ is modest over the full range of n_{emsignal}, with

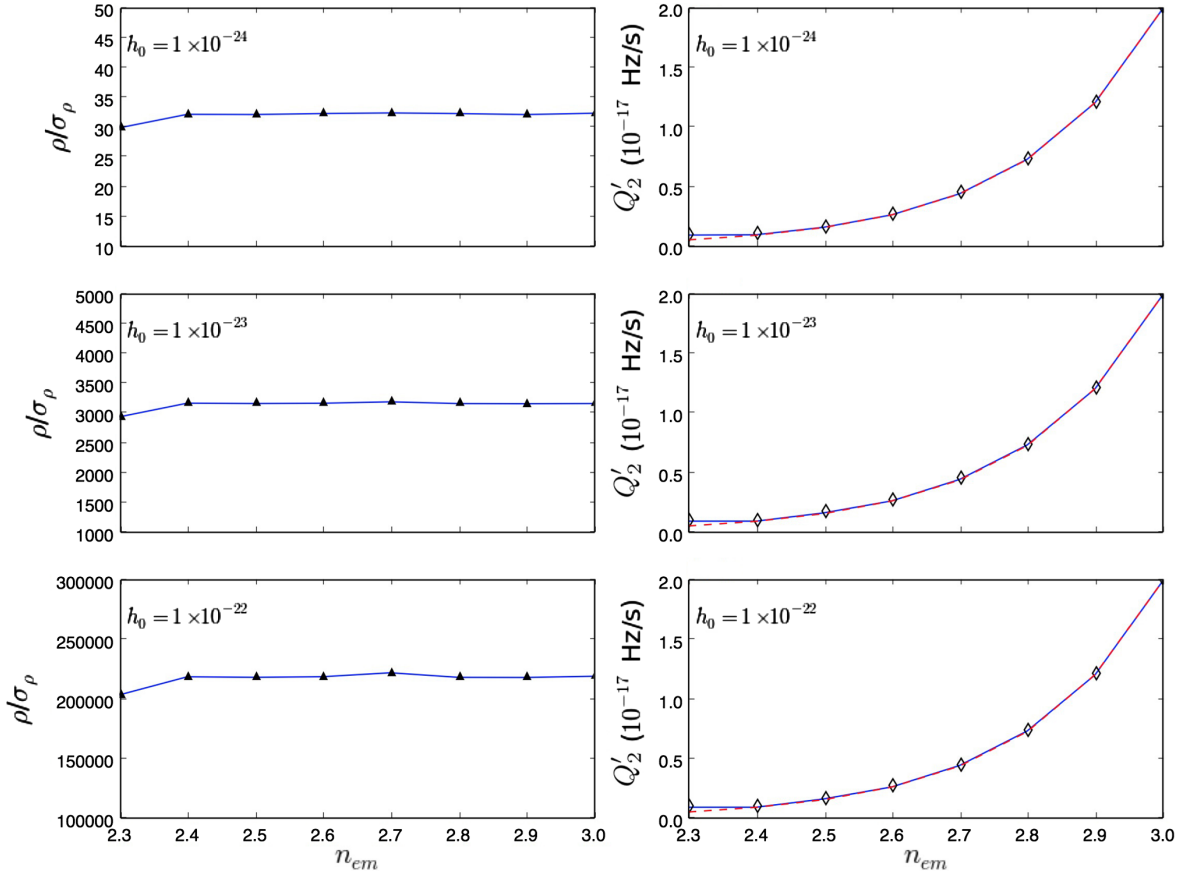

FIG. 11. Maximum ρ/σ_ρ (left) and equivalent Q_2' (right) obtained by fixing $n_{\rm em} = 3$, averaged over 100 trials, as functions of the true, injected electromagnetic braking index $n_{\rm emsignal}$ for (top to bottom) $h_0 = 1\times10^{-24}$, 1×10^{-23}, and 1×10^{-22} [$\sqrt{S_n(\nu)} = 3\times10^{-23}$ Hz$^{-1/2}$], with $\nu_{0\rm signal} = 150.1$ Hz and $Q_{2\rm signal} = 2\times10^{-17}$ Hz s^{-1}. The red dashed curves plot the theoretically predicted Q_2' from Eq. (27) as a function of $n_{\rm emsignal}$, which mainly overlap the empirical curves.

$(\rho/\sigma_\rho)_{\rm max} \simeq 32$, 3.2×10^3, 2.2×10^5 for $h_{0\rm signal} = 10^{-24}$, 10^{-23}, 10^{-22}, respectively. The reason why ρ/σ_ρ is always relatively lower for $n_{\rm emsignal} \simeq 2.3$ is that ρ/σ_ρ peaks at a smaller Q_2' value than the smallest one searched. We do not expand the Q_2 band to such a small value because that would introduce a finer resolution and thus require a much larger number of templates. We also find that the Q_2' which maximizes ρ/σ_ρ shifts relative to the injected value according to

$$Q_2' = \nu_0^{-\Delta n_{\rm em}} Q_{2\rm signal}, \tag{27}$$

as expected from Taylor expanding Eq. (18) in $|\xi| T_{\rm lag}/T_{\rm age} \ll 1$. The red dashed curves overplotted in the right panels of Fig. 11 display the theoretically predicted Q_2' values as a function of $n_{\rm emsignal}$ from Eq. (27) at $\nu_{0\rm signal} = 150.1$ Hz and $Q_{2\rm signal} = 2\times10^{-17}$ Hz s^{-1}. They are consistent with the empirical

TABLE VI. Injection parameters used to create the synthetic data analyzed in Sec. IV D 3 to study braking index evolution. Three values of h_0 and eight values of $n_{\rm emsignal}$ are chosen.

Injection parameter	Value	Units
$\nu_{0\rm signal}$	150.1	Hz
$Q_{1\rm signal}$	3.5×10^{-19}	Hz s^{-1}
$Q_{2\rm signal}$	2×10^{-17}	Hz s^{-1}
$\sqrt{S_n(\nu)}$	3×10^{-23}	Hz$^{-1/2}$
h_0	10^{-24}, 10^{-23}, 10^{-22}	
$n_{\rm emsignal}$	2.3, 2.4, 2.5, 2.6, 2.7, 2.8, 2.9, 3.0	

TABLE VII. Search parameter ranges for the targets in Table VI with $T_{\rm lag} = 3600$ s. The electromagnetic braking index $n_{\rm em} = 3$ is held fixed in every search.

Search parameter	Range	Resolution	Units
ν_0	149.6–150.6	0.01	Hz
Q_1	$3.0\times10^{-19} - 3.9\times10^{-19}$	0.1×10^{-19}	Hz s^{-1}
Q_2	$1.0\times10^{-18} - 2.5\times10^{-17}$	0.1×10^{-18}	Hz s^{-1}

results. This fact makes it possible to fix $n_{\rm em} = 3$ in the search, taking only Q_1 and Q_2 as spin-down variables and reducing $N_{\rm total}$ without sacrificing sensitivity.

V. SENSITIVITY

In this section, we present Monte Carlo tests to determine the smallest gravitational-wave signal detectable by the pipeline in Sec. III. Specifically, we empirically determine the value of $h_0^{\alpha_c}$, for which a fraction α_c (normally $\alpha_c = 0.95$) of the Monte Carlo trials yield $\rho/\sigma_\rho \geq \rho_{\rm th}$, where $\rho_{\rm th}$ is the agreed detection threshold. We discuss the choice of $\rho_{\rm th}$ in Sec. V A and estimate $h_0^{\alpha_c}$ in Secs. V B–V D.

A. Threshold $\rho_{\rm th}$

For a given false alarm rate α_f, $\rho_{\rm th}$ is estimated as follows. SFTs containing pure noise are generated, and a search is run over signal parameters (i.e., ν_0, Q_1, Q_2, and $n_{\rm em}$). The value of ρ/σ_ρ which yields a fraction α_f of positive detections is then $\rho_{\rm th}$. In this paper, we consider $\alpha_f = 1\%$. Specifically, for 10^3 searches over pure noise, we adjust $\rho_{\rm th}$ such that 10 trials have $\rho/\sigma_\rho > \rho_{\rm th}$.

An analytic expression for $\rho_{\rm th}$ (before normalizing by σ_ρ) given α_f and σ_ρ is presented by Dhurandhar *et al.* [12], viz.

$$\rho_{\rm th} = \sqrt{2}\sigma_\rho {\rm erfc}^{-1}(2\alpha_f/N_{\rm total}), \tag{28}$$

where erfc is the complementary error function, and $N_{\rm total}$ is the number of search templates. As shown in Sec. IV A, for pure noise, the PDF of ρ/σ_ρ is a Gaussian with zero mean and unit variance, assuming that all pairs are independent. As foreshadowed in Secs. IV A and IV B, we do not discuss the non-Gaussian corrections caused by dependent pairs in this paper because they are negligible for

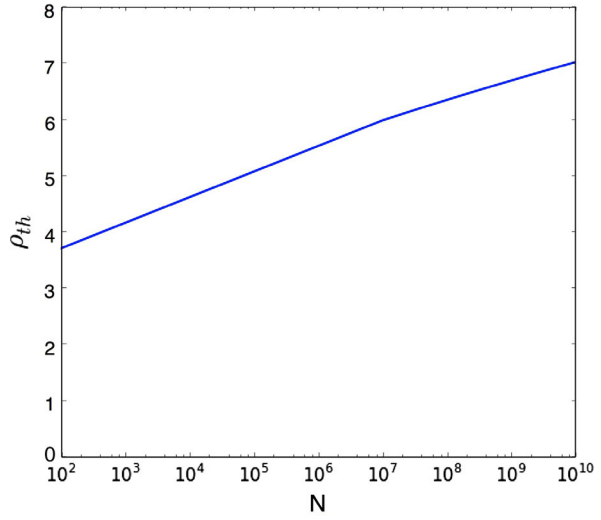

FIG. 12. Analytic detection threshold $\rho_{\rm th}$ as a function of $N_{\rm total}$ from Eq. (29) with $\alpha_f = 1\%$ and $\sigma_\rho = 1$.

TABLE VIII. Monte Carlo detection threshold $\rho_{\rm th}$ for three 0.1-Hz bands when searching pure noise, assuming zero spin-down, $N_{\rm total} = 10^3$, and $\alpha_f = 1\%$. Equation (29) yields $\rho_{\rm th} = 4.265$ analytically.

Band (Hz)	$\rho_{\rm th}$
150.0–150.1	4.440
300.0–300.1	4.433
600.0–600.1	4.516

$T_{\rm obs} = 1$ yr; for more details, see Ref. [69]. Hence the threshold reduces to

$$\rho_{\rm th} \approx F^{-1}[1 - (\alpha_f/N_{\rm total})], \tag{29}$$

where $F^{-1}(x)$ is the inverse cumulative distribution function (CDF) of x. Figure 12 plots $\rho_{\rm th}$ as a function of $N_{\rm total}$ from Eq. (29); it ranges from 3.72 for $N = 10^2$ to 7.03 for $N = 10^{10}$.

Searches without and with spin-down require different numbers of templates.

1. Pure noise, zero-spin-down search

The signal power is concentrated within one frequency bin when searching for a zero-spin-down signal. We therefore search 0.1-Hz bands centered on 150.05, 300.05, and 600.05 Hz, respectively, with a resolution of 10^{-4} Hz using SFTs containing only noise. Each trial consists of $N_{\rm total} = 10^3$ search templates. For $\alpha_f = 1\%$ and $\sigma_\rho = 1$, Eq. (29) yields $\rho_{\rm th} = 4.265$. For each band searched, we adjust $\rho_{\rm th}$ such that it is exceeded by only 10 out of 10^3 of the ρ/σ_ρ values. Table VIII lists $\rho_{\rm th}$ for the three bands. The result in each band agrees with the analytic value to better than 6%.

2. Pure noise, spin-down search

Searching for a spinning-down signal involves more parameters (i.e., Q_1, Q_2, $n_{\rm em}$) and hence larger $N_{\rm total}$. Here, we consider the parameter space defined in Table IX. Each trial consists of $N_{\rm total} = 100 \times 7 \times 11 = 7700$ search templates. The analytic estimate from Eq. (29) yields

TABLE IX. Search parameter ranges used to estimate the threshold for a spin-down search in Sec. V A 2 with $n_{\rm em} = 3$ fixed. The data contain Gaussian noise ($h_0 = 0$). The ranges of Q_1 and Q_2 correspond to 7.6×10^{-9} Hz s^{-1} $\leq |\dot{\nu}| \leq 5.3 \times 10^{-8}$ Hz s^{-1}, $2.4 \times 10^{-4} \leq \epsilon \leq 6.4 \times 10^{-4}$, and 1.3×10^{11} G $\leq B \leq 4.2 \times 10^{11}$ G.

Search parameter	Range	Resolution	Units
ν_0	150.0–150.1	10^{-3}	Hz
Q_1	$1.0 \times 10^{-19} - 7.0 \times 10^{-19}$	1×10^{-19}	Hz s^{-1}
Q_2	$1.0 \times 10^{-18} - 1.1 \times 10^{-17}$	1×10^{-18}	Hz s^{-1}

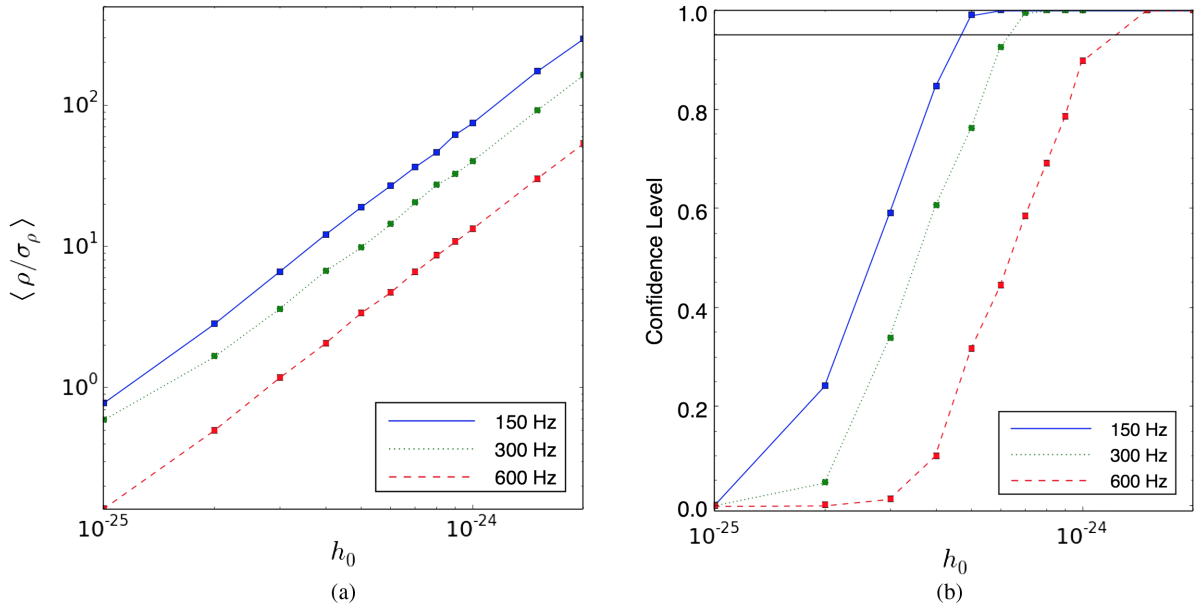

FIG. 13. Sensitivity without spin-down. (a) Normalized detection statistic $\langle \rho/\sigma_\rho \rangle$ averaged over 10^3 trials, and (b) confidence level C, as functions of injected gravitational-wave strain h_0. The injected signals have random $\cos\iota_{\text{signal}}$ and ψ_{signal}, fixed sky positions $(\alpha, \delta) = (1.46375 \text{ rad}, -1.20899 \text{ rad})$, and $\nu_{0\text{signal}} = 150.05$ Hz (solid curve), 300.05 Hz (dotted curve), and 600.05 Hz (dashed curve). For each injected frequency, ρ_{th} is listed in Table VIII for $N_{\text{total}} = 10^3$. The horizontal line in (b) indicates $C = 0.95$.

$\rho_{\text{th}} = 4.700$. Results from the Monte Carlo tests, adjusting ρ_{th} to be exceeded by only 10 out of 10^3 of the ρ/σ_ρ values, yield $\rho_{\text{th}} = 4.898$, which is 4% larger than the analytic estimate.

B. Sensitivity for zero-spinning-down signals

Without considering the spin-down of a signal, we determine $h_0^{95\%}$ using ρ_{th} from Table VIII.

We inject signals with constant $\nu_{0\text{signal}} = 150.05$, 300.05, and 600.05 Hz and strains in the range $1 \times 10^{-25} \leq h_0 \leq 2 \times 10^{-24}$ into 1 year of 30-min SFTs from H1 and L1, with signal parameters $(\alpha, \delta) = (1.46375, -1.20899)$ (the coordinates of SNR 1987A), random $\cos\iota_{\text{signal}}$ and ψ_{signal}, and $S_n(\nu)$ given by Eq. (21). We then search a 0.1-Hz band centered on $\nu_{0\text{signal}}$ with a resolution of 10^{-4} Hz, using the exact sky position (α, δ) and averaging over $\cos\iota$ and ψ ($T_{\text{lag}} = 3600$ s). The normalized detection statistic $\langle \rho/\sigma_\rho \rangle$ averaged over 10^3 trials is plotted as a function of h_0 in Fig. 13. The solid, dotted, and dashed lines correspond to $\nu_{0\text{signal}} = 150.05$ Hz, 300.05 Hz, and 600.05 Hz, respectively. As expected, $\langle \rho/\sigma_\rho \rangle$ grows $\propto h_0^2$ from Eq. (24) for a given $\nu_{0\text{signal}}$, and it drops when $\nu_{0\text{signal}}$ and hence $\sqrt{S_n}$ increase. In Fig. 13(b), we plot the confidence level C (i.e., the fraction of ρ/σ_ρ values, in each set of 10^3 trials, which exceed ρ_{th}) as a function of h_0. Linear interpolation in Fig. 13(b) implies that C increases to $\geq 95\%$ for $h_0 \geq h_0^{95\%}$ for the $h_0^{95\%}$ values listed in Table X.

The results interpolated from Fig. 13(b) are for a search over 10^3 templates. The full search involves $\sim 10^9$ templates, corresponding to $\rho_{\text{th}} \approx 6.71$ from Eq. (29). The estimated strain limits, which are ~20% larger, appear in the lower half of Table X.

TABLE X. Wave strain threshold $h_0^{95\%}$ (i.e., confidence $C \geq 0.95$) estimated for three 0.1-Hz bands containing pure Gaussian noise. For $N_{\text{total}} = 10^3$, the thresholds are estimated from linear interpolation of Monte Carlo simulation results plotted in Fig. 13(b). For $N_{\text{total}} = 10^9$, the thresholds are based on analytical estimation from Eq. (29).

N_{total}	$\nu_{0\text{signal}}$ (Hz)	$h_0^{95\%}$
10^3	150.05	4.72×10^{-25}
	300.05	6.36×10^{-25}
	600.05	1.26×10^{-24}
10^9	150.05	5.64×10^{-25}
	300.05	7.60×10^{-25}
	600.05	1.42×10^{-24}

TABLE XI. Injection parameters used to create the synthetic data analyzed in Sec. V C containing spinning-down signals. The injection parameters $Q_{1\text{signal}}$ and $Q_{1\text{signal}}$ are computed from the astrophysical parameters using Eqs. (17) and (18). The corresponding initial spin-down rate $|\dot{\nu}(0)|$ is 3.81×10^{-8} Hz s^{-1}.

Injection parameter	Value	Astrophysical parameter
$\nu_{0\text{signal}}$	150.05 Hz	
$Q_{1\text{signal}}$	5×10^{-19} Hz s^{-1}	$\epsilon = 5.4 \times 10^{-4}$
$Q_{2\text{signal}}$	1×10^{-17} Hz s^{-1}	$B = 4.05 \times 10^{11}$ G

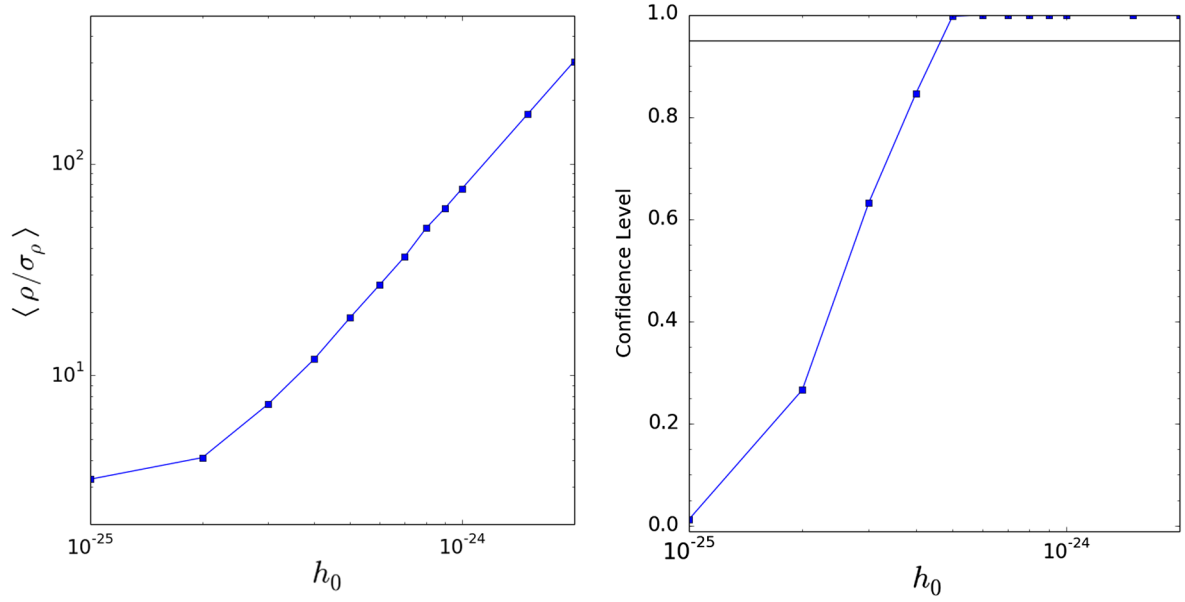

FIG. 14. Sensitivity with spin-down ($\nu_{0\text{signal}} = 150.05$ Hz, $Q_{1\text{signal}} = 5 \times 10^{-19}$ Hz s^{-1}, $Q_{2\text{signal}} = 1 \times 10^{-17}$ Hz s^{-1}). (a) Normalized detection statistic $\langle \rho/\sigma_\rho \rangle$ averaged over 10^3 trials, and (b) confidence level C, as functions of injected gravitational-wave strain h_0. The injected signals have random $\cos\iota_{\text{signal}}$ and ψ_{signal} and fixed sky positions $(\alpha, \delta) = (1.46375 \text{ rad}, -1.20899 \text{ rad})$. The horizontal line in (b) indicates $C = 0.95$.

C. Sensitivity for spinning-down signals

We inject spin-down signals with the parameters quoted in Table XI. The wave strain is still in the range $1 \times 10^{-25} \leq h_0 \leq 2 \times 10^{-24}$, and all other parameters remain the same as those in Sec. V B. The same searches with 10^3 templates are carried out, and the normalized detection statistics averaged over 10^3 trials, as well as the confidence levels, are shown in Fig. 14. Despite the signal spin-down, the values of $\langle \rho/\sigma_\rho \rangle$ [Fig. 14(a)] and C [Fig. 14(b)] are close to those plotted in Fig. 13 at the same h_0. Hence, we find a similar $h_0^{95\%} \sim 4.72 \times 10^{-25}$.

D. Sensitivity for spinning-down signals with limitation on h_0

The search sensitivity depends on two factors: (1) spin-down rate (i.e., combination of spin-down parameters ν_0, Q_1, Q_2, and n_{em}) and (2) wave strain h_0. First, the cross-correlation pipeline tracks up to $\nu^{(6)}(t)$ terms using the astrophysical model, so the search is most sensitive for the regime with spin-down rate $|\dot{\nu}(0)| \lesssim 10^{-7}$ Hz s^{-1}, above which the sensitivity starts to drop quickly because the error in tracked signal phase increases to $\gtrsim \pi/2$ after 1 year's observation. Second, given ϵ and ν, the gravitational-wave strain at Earth is [64]

$$h_0 = \frac{4\pi^2 G}{c^4} \frac{I\epsilon\nu^2}{D}. \tag{30}$$

A stronger signal indicates larger ϵ and ν_0 and hence a higher spin-down rate, which inversely decreases the sensitivity.

We first inject spin-down signals with the parameters quoted in Table XII into 1 year of 30-min SFTs from H1 and L1. Wave strain is in the range $1 \times 10^{-25} \lesssim h_0 \lesssim 7 \times 10^{-25}$

TABLE XII. Injection parameters used to create the first set of synthetic data analyzed in Sec. V D containing spinning-down signals, in which $Q_{2\text{signal}}$ is fixed and a group of $Q_{1\text{signal}}$ values are tested. The corresponding astrophysical parameters ϵ and B in Eq. (17) are also quoted in the last column. The wave strain covers the range $1 \times 10^{-25} \lesssim h_0 \lesssim 7 \times 10^{-25}$ as calculated from Eq. (30).

Injection parameter	Value	Astrophysical parameter
$\nu_{0\text{signal}}$	150.05 Hz	
$Q_{1\text{signal}}$	$1 \times 10^{-19} - 4 \times 10^{-18}$ Hz s^{-1}	$2.4 \times 10^{-4} \leq \epsilon \leq 1.5 \times 10^{-3}$
$Q_{2\text{signal}}$	1×10^{-17} Hz s^{-1}	$B = 4.05 \times 10^{11}$ G
n_{emsignal}	3	

TABLE XIII. Search parameter ranges for injected spin-down signals in Tables XII and XIV. The ranges are centered on the injected signals. The range width column defines the domain of the search parameter assuming that it is centered on the injection.

Search parameter	Range width	Resolution	Units
ν_0	0.1	10^{-3}	Hz
Q_1	7×10^{-19}	1×10^{-19}	$\mathrm{Hz\,s^{-1}}$
Q_2	1.1×10^{-17}	1×10^{-18}	$\mathrm{Hz\,s^{-1}}$

by using Eq. (30).[5] We search the parameter ranges in Table XIII. We have $\rho_{\mathrm{th}} = 4.898$ for a signal with $\nu_{0\mathrm{signal}} = 150.05$ Hz in Sec. V A 2, given $N_{\mathrm{total}} = 7700$. Figure 15 plots the normalized detection statistic $\langle \rho/\sigma_\rho \rangle$ averaged over 10^3 trials as a function of $Q_{1\mathrm{signal}}$ (bottom axis) and corresponding ϵ (top axis). We plot the confidence level C as a function of $Q_{1\mathrm{signal}}$ and ϵ in Fig. 15(b). The confidence level C increases with $Q_{1\mathrm{signal}}$ and ϵ but saturates at $\sim$0.9 for $Q_{1\mathrm{signal}} \gtrsim 2 \times 10^{-18}$ $\mathrm{Hz\,s^{-1}}$ $[|\dot{\nu}(0)| \sim 1.5 \times 10^{-7}$ $\mathrm{Hz\,s^{-1}}]$. This result is consistent with our expectation that, as h_0 increases, larger ϵ and ν_0 (i.e., higher spin-down rate) lead to difficulty in phase tracking and prevent achieving better sensitivity.

Next we inject signals with the parameters quoted in Table XIV. This time we fix $Q_{1\mathrm{signal}}$ and test a group of $Q_{2\mathrm{signal}}$ values for the same ranges as in Table XIII. Figure 16 plots the normalized detection statistic $\langle \rho/\sigma_\rho \rangle$ averaged over 10^3 trials as a function of $Q_{2\mathrm{signal}}$ (bottom axis) and corresponding B (top axis). As expected, varying $Q_{2\mathrm{signal}}$ within a reasonable range of magnetic field strength does not impact the sensitivity much for given $Q_{1\mathrm{signal}}$ because the wave strain depends more on ϵ than B.

VI. LIGO S5 SEARCH

A. Data and templates

The S5 data contain 2 years of SFTs, collected from November 2005 to October 2007. A search of the band 75–450 Hz is conducted, using SFTs from the H1 and L1 interferometers from 01 November 2006 to 30 October 2007 UTC. The second year of S5 is chosen because we are limited computationally to $T_{\mathrm{obs}} \leq 1$ year, and the noise power spectral density is lower during the second year than the first. We analyze 23 223 30-min SFTs in total, with 12 590 from H1 and 10 633 from L1.

In view of the substantial computational cost, we select the template grid with an eye towards efficiency. In Sec. VI of Ref. [8], a semicoherent phase metric was developed to calculate the mismatch m as a function of the template spacing along each of the four axes of the parameter space (ν_0, Q_1, Q_2, n_{em}). For the search in this paper, we elect to tolerate a maximum mismatch $m \leq 0.2$ for the template closest to the true source parameters. Drawing on the analysis in Sec. VI of Ref. [8], specifically Eqs. (39)–(41), we construct a set of templates $\{\nu_0, Q_1, Q_2\}$ across the astrophysically relevant parameter range quoted in Table XV. The largest values of Q_1 and Q_2 are limited by the maximum number of templates we can afford computationally ($N_{\mathrm{total}} \sim 10^9$). Only two values of Q_2 are needed to sample the relevant range at the resolution required for $m \leq 0.2$. We fix $n_{\mathrm{em}} = 3$ (see Sec. IV D 3), the sky position $(\alpha, \delta) = (1.46375, -1.20899)$, and $T_{\mathrm{lag}} = 3600$ s, and average over $\cos\iota$ and ψ. As the pipeline loses track of the signal phase quickly with a spin-down rate $|\dot{\nu}(0)| \gtrsim 10^{-7}$ $\mathrm{Hz\,s^{-1}}$ (see Sec. V D), a narrower band of Q_1 is searched for $350 \leq \nu_0/\mathrm{Hz} \leq 450$. The total number of templates is $N_{\mathrm{total}} = 2,373,875,000$, implying $\rho_{\mathrm{th}} \approx 6.50 (\alpha_{\mathrm{f}} = 10\%)$.

B. Candidates and line vetoes

Templates $\{\nu_0, Q_1, Q_2\}$ with $\rho/\sigma_\rho > \rho_{\mathrm{th}}$ are found to cluster at 19 narrow ν_0 bands, each spanning $\sim$0.5 Hz and extending over the entire ranges of Q_1 and Q_2. We list the peak ρ and corresponding ν_0, Q_1, and Q_2 values in Table XVI for each cluster.

Continuous waves emitted by nonspherical spinning neutron stars appear as narrow spectral lines. The instrumental power line at 60 Hz with wings extending ± 2 Hz, its harmonics, and noise lines from electronics, wire, calibration, etc., impact the search by obscuring astrophysical signals in that band. Within the frequency range we are searching, the most prominent known peaks lie at low frequencies, $\sim$90–100 Hz (electronic lines), and at $\sim$329–350 Hz (mirror suspensions). An instrumental line catalog can be found in Appendix B of Ref. [71] and at the LIGO Open Science Center.[6] We notch out bands contaminated by known noise lines. For each candidate cluster with a peak at frequency ν_0 and $\dot{\nu}_0$ (calculated from Q_1 and Q_2), we veto the cluster if the band $\nu_0 - \Delta\nu \leq \nu \leq \nu_0 + \Delta\nu$, with $\Delta\nu \approx \nu_0 \times 10^{-4} + |\dot{\nu}_0| \times 3.14 \times 10^7$ s, overlaps with a known noise line. This criterion takes into account the maximum possible Doppler shift due to the Earth's orbit and the maximum frequency shift due to the spin-down of the source [71]. The surviving candidates are listed in Table XVII.

C. Manual vetoes

We now examine the survivors in Table XVII manually to check if they are false alarms. We do this in two ways. First, we search the second year of S5 (01 November 2006 to 30 October 2007 UTC) from H1 and L1 separately to test

[5]For comparison, we have $h_0 = 2.5 \times 10^{-25}$ computed from Eq. (30) using parameters quoted in Table XI in Sec. V C, which is relatively low compared to the range $1 \times 10^{-25} \lesssim h_0 \lesssim 7 \times 10^{-25}$ we test in Sec. V D.

[6]https://losc.ligo.org/speclines/

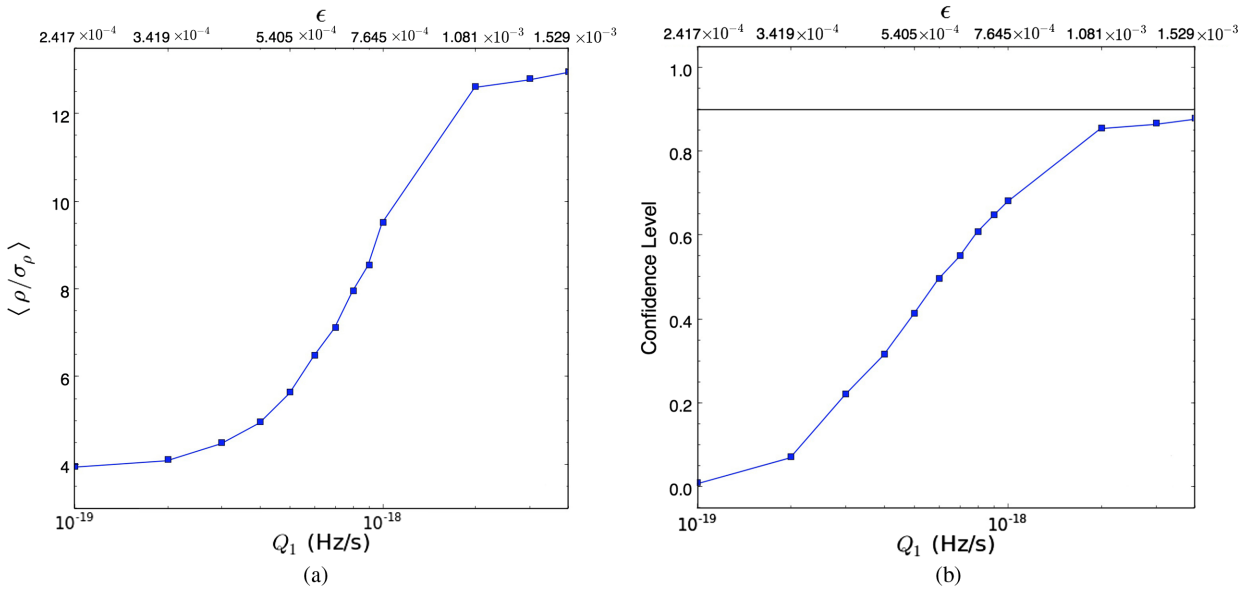

FIG. 15. Sensitivity with spin-down. (a) Normalized detection statistic $\langle \rho/\sigma_\rho \rangle$ averaged over 10^3 trials and (b) confidence level C as functions of $Q_{1\mathrm{signal}}$ (bottom axis) and ϵ (top axis). The injected signals have random $\cos\iota_{\mathrm{signal}}$ and ψ_{signal}, fixed sky positions $(\alpha, \delta) = (1.46375\ \mathrm{rad}, -1.20899\ \mathrm{rad})$, $\nu_{0\mathrm{signal}} = 150.05$ Hz, and $Q_{2\mathrm{signal}} = 1 \times 10^{-17}\ \mathrm{Hz\,s^{-1}}$. From Sec. V A 2, we set $\rho_{\mathrm{th}} = 4.898$ for $N_{\mathrm{total}} = 7700$. The horizontal line in (b) indicates $C = 0.90$.

if the signal appears in both interferometers. The sensitivities of the two interferometers during S5 are comparable to one another, implying that a signal is expected to meet the same detection criterion in both detectors. Second, we search the first year of S5 (04 November 2005 to 30 October 2006 UTC) from H1 and L1 to test if the candidate persists in both years. As with the first detection criterion, the strain sensitivities of the detectors in the first and second years of observation are comparable, implying that a gravitational-wave signal present in one year of data should also be present in both.

Figure 17 compares the output from both detectors (H1 and L1; top two panels in each group of four) and from one detector (H1 or L1; bottom two panels in each group of four) for each candidate cluster. For clusters (a) and (b), the bottom two panels are from H1 and no detection is found in L1; for (c), (d), and (e), the bottom two panels are from L1 and no detection is found in H1. The left panels in each group of four are for $Q_2 = 1 \times 10^{-21}\ \mathrm{Hz\,s^{-1}}$, and the right

TABLE XIV. Injection parameters used to create the second set of synthetic data analyzed in Sec. V D containing spinning-down signals, in which $Q_{1\mathrm{signal}}$ is fixed and a group of $Q_{2\mathrm{signal}}$ values are tested. The corresponding astrophysical parameters ϵ and B in Eq. (17) are also quoted in the last column. The wave strain $h_0 = 3 \times 10^{-25}$ is calculated from Eq. (30).

Injection parameter	Value	Astrophysical parameter
$\nu_{0\mathrm{signal}}$	150.05 Hz	
$Q_{1\mathrm{signal}}$	$7 \times 10^{-19}\ \mathrm{Hz\,s^{-1}}$	$\epsilon = 6.4 \times 10^{-4}$
$Q_{2\mathrm{signal}}$	$2 \times 10^{-18} - 1 \times 10^{-16}\ \mathrm{Hz\,s^{-1}}$	$1.8 \times 10^{11}\ \mathrm{G} \le B \le 1.3 \times 10^{12}\ \mathrm{G}$
n_{emsignal}	3	

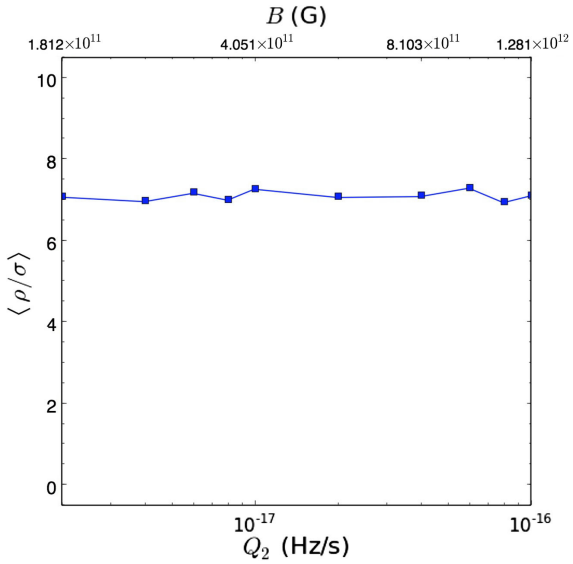

FIG. 16. Normalized detection statistic $\langle \rho/\sigma_\rho \rangle$ averaged over 10^3 trials as a function of Q_1 (bottom axis) and magnetic field strength B (G) (top axis). The injected signals have random $\cos\iota_{\mathrm{signal}}$ and ψ_{signal}, fixed sky positions $(\alpha, \delta) = (1.46375\ \mathrm{rad}, -1.20899\ \mathrm{rad})$, $\nu_{0\mathrm{signal}} = 150.05$ Hz, and $Q_{1\mathrm{signal}} = 7 \times 10^{-19}\ \mathrm{Hz\,s^{-1}}$.

TABLE XV. Ranges and resolutions of template parameters ν_0, Q_1, and Q_2 ($n_{\rm em}$ fixed). Only two Q_2 values are searched. Corresponding ranges of ϵ and B are listed in the right column.

ν_0 (Hz)	Resolution (Hz)	Q_1, Q_2(Hz/s)	Resolution (Hz/s)	ϵ, $B(G)$
$75 \le \nu_0 < 350$	4×10^{-4}	$2 \times 10^{-22} \le Q_1 \le 6.17 \times 10^{-19}$	3.68×10^{-22}	$1.08 \times 10^{-5} \le \epsilon \le 6.0 \times 10^{-4}$
		$1 \times 10^{-21} \le Q_2 \le 2 \times 10^{-16}$	2×10^{-16}	$4.05 \times 10^{9} \le B \le 1.81 \times 10^{12}$
$350 \le \nu_0 \le 450$	4×10^{-4}	$2 \times 10^{-22} \le Q_1 \le 4.99 \times 10^{-20}$	3.68×10^{-22}	$1.08 \times 10^{-5} \le \epsilon \le 1.71 \times 10^{-4}$
		$1 \times 10^{-21} \le Q_2 \le 2 \times 10^{-16}$	2×10^{-16}	$4.05 \times 10^{9} \le B \le 1.81 \times 10^{12}$

panels are for $Q_2 = 2 \times 10^{-16}$ Hz s^{-1}. Red and blue dots stand for ρ higher and lower than 50, respectively. In some cases, the cluster spreads wider across parameter space ν_0, Q_1, and ρ/σ_ρ is higher from the output of one detector than from both detectors because the loud noise line causing these candidates in one detector is weakened by the noise in the other detector.

The only candidate seen in both detectors lies around 112 Hz. The detection statistic ρ/σ_ρ for this candidate is plotted as a dot for each template $\{\nu_0, Q_1, Q_2\}$ with $\rho/\sigma_\rho > \rho_{\rm th} = 6.5$ in Fig. 18. At $Q_2 = 1 \times 10^{-21}$ Hz s^{-1}, three templates exceed $\rho_{\rm th}$ obtained using both detectors, five templates exceed $\rho_{\rm th}$ for H1, and one template exceeds $\rho_{\rm th}$ for L1. No hits are at $Q_2 = 2 \times 10^{-16}$ Hz s^{-1}. Following up further, we take the first year of S5 data from H1 and L1 and run the same search around 112 Hz. If the candidate is astrophysical in origin, we expect a detection with similar statistical significance at a slightly higher ν_0 consistent with the astrophysical spin-down model. However, nothing is detected in the first year of S5 data for $111.5 \le \nu_0/{\rm Hz} \le 112.5$, $2 \times 10^{-22} \le Q_1/{\rm Hz\,s^{-1}} \le 6.17 \times 10^{-19}$, and $1 \times 10^{-21} \le Q_2/{\rm Hz\,s^{-1}} \le 2 \times 10^{-16}$. As the candidate comprises relatively few templates, and ρ/σ_ρ stands just above the threshold, a false alarm is strongly implied.

In summary, no candidate survives the manual vetoes. The false alarm rate selected for the whole search is 10%, so a single false alarm candidate cluster is consistent with our expectation.

To better understand the cause of the strongest vetoed candidates (i.e., clusters around 91 Hz and 381 Hz; both found in L1), we divide the second year of S5 data from the L1 detector into two halves (01 November 2006 to 30 April 2007 UTC and 01 May 2007 to 30 October 2007 UTC), search them separately, and compare the two outputs. The cluster around 91 Hz only exists in the second half of the year. The cluster around 381 Hz only exists in the first half of the year. The normalized detection statistic for each template $\{\nu_0, Q_1, Q_2\}$ with $\rho/\sigma_\rho > \rho_{\rm th} = 6.5$ from L1 is plotted in Fig. 19 [(a) for a cluster around 91 Hz in the second half of the year, and (b) for a cluster around 381 Hz in the first half of the year]. The patterns of dots in the (Q_1, ν_0) plane from the second half of the year [around 91 Hz; Fig. 19] and the first half of the year [around 381 Hz; Fig. 19(b)] are exactly the same as those from the whole year [see Figs. 17(c) and 17(e)]. Hence, instead of being some persistent noise line throughout the whole observation period, the candidate is probably a short-term glitch.

We also check how the pattern of dots caused by a glitch differs from that of a known instrumental spectral line. We

TABLE XVI. First-pass candidates from the LIGO S5 search for SNR 1987A, listing the maximum ρ/σ_ρ in each cluster with $\rho/\sigma_\rho > \rho_{\rm th} = 6.50$ and the corresponding ν_0, Q_1, and Q_2, sorted according to ν_0.

ρ/σ_ρ	ν_0 (Hz)	Q_1(Hz s^{-1})	Q_2(Hz s^{-1})
23.81	75.0240	1.0872×10^{-20}	1×10^{-21}
3774.10	91.1360	1.80888×10^{-19}	1×10^{-21}
7.77	93.2896	2.20264×10^{-19}	2×10^{-16}
11.07	96.4980	2.31304×10^{-19}	2×10^{-16}
35.73	100.0008	1.0136×10^{-20}	1×10^{-21}
90.11	108.8632	5.0984×10^{-20}	1×10^{-21}
10.90	112.0000	2.408×10^{-21}	1×10^{-21}
47.07	119.8792	4.984×10^{-21}	1×10^{-21}
27.73	128.0012	4.616×10^{-21}	1×10^{-21}
49.61	139.5112	2.776×10^{-21}	1×10^{-21}
7.72	144.8112	1.31944×10^{-19}	2×10^{-16}
7.26	145.3072	5.64344×10^{-19}	1×10^{-21}
21.89	179.8132	9.36×10^{-22}	1×10^{-21}
23.93	193.5700	4.3256×10^{-20}	1×10^{-21}
8.22	200.0304	9.032×10^{-21}	2×10^{-16}
7.79	329.7820	2.00×10^{-22}	1×10^{-21}
2891.52	381.9036	2.040×10^{-21}	1×10^{-21}
1093.79	393.1372	9.36×10^{-22}	1×10^{-21}
6243.65	396.9736	9.36×10^{-22}	1×10^{-21}

TABLE XVII. Second-pass candidates from the LIGO S5 search for SNR 1987A after instrumental line veto, listing the maximum ρ/σ_ρ in each cluster with $\rho/\sigma_\rho > \rho_{\rm th} = 6.50$ and the corresponding ν_0, Q_1, and Q_2, sorted according to ν_0.

ρ/σ_ρ	ν_0 (Hz)	Q_1(Hz s^{-1})	Q_2(Hz s^{-1})
3774.10	91.1360	1.80888×10^{-19}	1×10^{-21}
35.73	100.0008	1.0136×10^{-20}	1×10^{-21}
10.90	112.0000	2.408×10^{-21}	1×10^{-21}
27.73	128.0012	4.616×10^{-21}	1×10^{-21}
8.22	200.0304	9.032×10^{-21}	2×10^{-16}
2891.52	381.9036	2.040×10^{-21}	1×10^{-21}

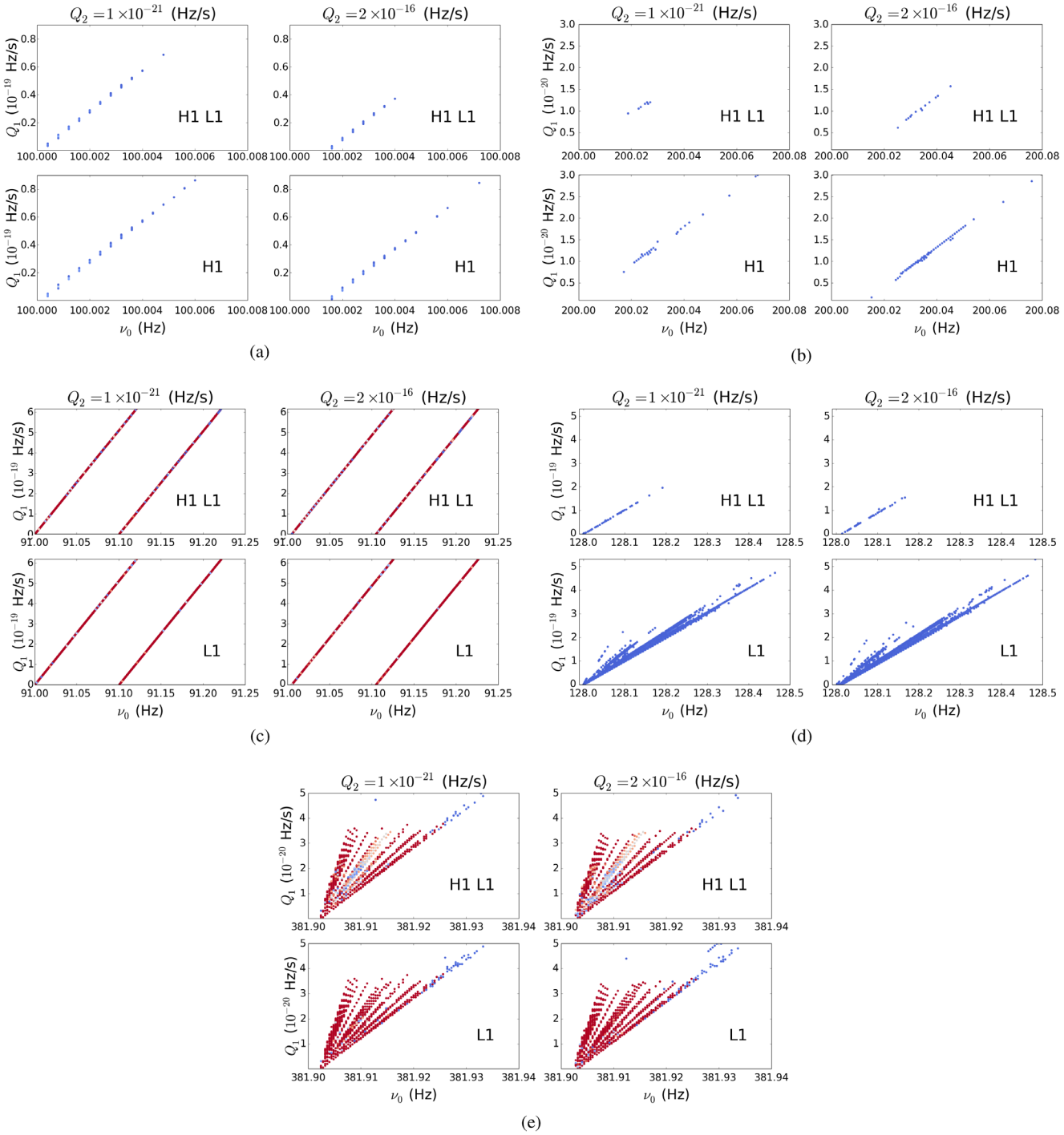

FIG. 17. Surviving candidates after instrumental line veto. Normalized detection statistic ρ/σ_ρ as a function of Q_1 and ν_0 for five clusters (group of four panels). Each dot on the plots stands for one template $\{\nu_0, Q_1, Q_2\}$ with $\rho/\sigma_\rho > \rho_{\rm th} = 6.5$. The color of the dots indicates values of ρ/σ_ρ (larger ρ/σ_ρ in warmer colors). The dots merge into continuous lines or thick bars because they are closely spaced. For each cluster, two values of Q_2 are searched: $Q_2 = 1 \times 10^{-21}$ Hz s^{-1} (left two panels in each group of four) and $Q_2 = 2 \times 10^{-16}$ Hz s^{-1} (right two panels in each group of four). The top and bottom panels in each group correspond to two detectors (H1 and L1) and one detector (H1 or L1), respectively. For clusters (a) and (b), no detection is found in L1; for (c), (d), and (e), no detection is found in H1.

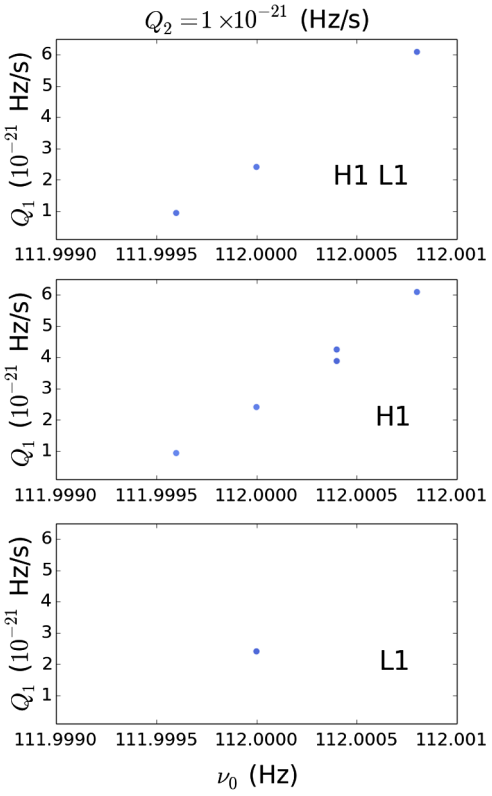

FIG. 18. Surviving candidate cluster around 112 Hz seen in both detectors. Normalized detection statistic ρ/σ_ρ as a function of Q_1 and ν_0. Each dot on the plots stands for one template $\{\nu_0, Q_1, Q_2\}$ with $\rho/\sigma_\rho > \rho_{\rm th} = 6.5$. All templates are obtained at $Q_2 = 1 \times 10^{-21}$ Hz s^{-1}, and no hits are at $Q_2 = 2 \times 10^{-16}$ Hz s^{-1}. The top, middle, and bottom panels correspond to two detectors (H1 and L1), H1, and L1, respectively.

plot two examples of the clusters caused by instrumental lines at 108.8 Hz and 193.4 Hz in Fig. 20. We find that the pattern of dots is similar to a glitch, with dots spreading ~0.5 Hz in frequency across the whole Q_1 and Q_2 band searched. Interestingly, therefore, we cannot differentiate reliably between a persistent line and a transient glitch from the super-threshold template distribution in the (Q_1, ν_0) plane.

D. Wave strain upper limit

Without a detection, we are able to place an upper limit on h_0 as a function of ν_0.

Given the one-sided power spectral density $S_n^{(1)}(\nu)$ and $S_n^{(2)}(\nu)$ for each interferometer, and assuming that ρ is normally distributed, the lowest detectable gravitational-wave strain $h_{\rm th}(\nu)$ calculated by Dhurandhar *et al.* [12] is

$$h_{\rm th}(\nu) = \frac{\mathcal{S}^{1/2}}{\sqrt{2}\langle|\tilde{\mathcal{G}}_{IJ}|^2\rangle^{1/4} N_{\rm pairs}^{1/4}} \left[\frac{(S_n^{(1)}(\nu) S_n^{(2)}(\nu))^{1/2}}{\Delta T}\right]^{1/2}, \tag{31}$$

with $\mathcal{S} = \mathrm{erfc}^{-1}(2\alpha_{\rm f}) + \mathrm{erfc}^{-1}(2\alpha_{\rm d})$, where $\alpha_{\rm f}$ is the false alarm rate, $\alpha_{\rm d}$ is the false dismissal rate, $\langle|\tilde{\mathcal{G}}_{IJ}|^2\rangle$ is the cross-correlation function defined in Eq. (5) averaged over $\cos\iota$ and ψ, and $N_{\rm pairs}$ is the number of SFT pairs. The theoretical sensitivity is analyzed as a function of ν_0 in Sec. 4 1 of Chung *et al.* [8], who found $h_0 \leq 1.6 \times 10^{-25}$ at the most sensitive frequency around 150 Hz, with $\alpha_{\rm f} = \alpha_{\rm d} = 0.1$. This estimate in Ref. [8] is also based on the S5 noise curve, and hence it is approximately the theoretical sensitivity we expect.

The upper limit we are able to place is more conservative than $h_{\rm th}$ in Eq. (31) because the sensitivity drops significantly for $|\dot{\nu}(0)| \gtrsim 10^{-7}$ Hz s^{-1} (i.e., large Q_1, Q_2, and ν_0), where the pipeline loses track of the signal phase ($\gtrsim \pi/2$) after a year's observation (see Sec. V D). The observation period during which the phase tracking remains accurate is shorter than 1 year for $|\dot{\nu}(0)| \gtrsim 10^{-7}$ Hz s^{-1}, reducing $N_{\rm pairs}$ and hence the sensitivity. At a given ν_0, when the largest Q_1 and Q_2 in our parameter space are set in the template, the search is least sensitive because of the largest $|\dot{\nu}(0)|$ leading to the quickest loss in phase tracking. Hence the upper limit on h_0 at this ν_0 is the most conservative with the largest Q_1 and Q_2. We analyze the upper limit on h_0 as a function of ν_0 with both the largest and smallest Q_1 and Q_2.

We first evaluate the upper limit on h_0 with the largest Q_1 and Q_2 values in the two frequency bands searched separately. The largest Q_1 and Q_2 values are listed in Table XVIII. At each given ν_0, we find the smallest h_0, above which we have $\rho/\sigma_\rho > \rho_{\rm th} = 6.5$ (i.e., a detection with 90% confidence level). Hence, this h_0 is the 90% confidence level upper limit without a detection.

The analysis is described in three steps. First, we inject synthetic signals for wave strains in the range $1 \times 10^{-25} \leq h_0 \leq 2 \times 10^{-24}$ spinning down with $Q_{1\max}$ and $Q_{2\max}$ in Table XVIII. Second, we search these synthetic data sets with the same templates as we use searching the LIGO S5 data in Sec. VI A, and we plot the normalized detection statistic ρ/σ_ρ as contours on the (h_0, ν_0) planes in Fig. 21 for two frequency ranges, respectively. Third, we draw the contour $\rho/\sigma_\rho = \rho_{\rm th} = 6.5$ as a red dashed curve. For given ν_0, any h_0 above the curve leads to $\rho/\sigma_\rho > \rho_{\rm th} = 6.5$, which stands for a detection with $\alpha_{\rm f} = \alpha_{\rm d} = 0.1$. Hence, the red dashed curve shows the 90% confidence level upper limits on h_0 given that no detection is found.

As the injected ν_0 gets larger, the sensitivity decreases and the upper limit on h_0 increases. Comparing Figs. 21(a) and 21(b) in the frequency range 255–300 Hz, the upper limit on h_0 is larger in panel (a) than in panel (b) by a factor of ~3. The lower upper limit on h_0 in panel (b) does not indicate better sensitivity because we sacrifice ~90% of the Q_1 parameter space compared to (a). Generally speaking, the pipeline is most sensitive for the parameter domain defined in Table XIX, reaching $h_0 \leq 8 \times 10^{-25}$. The best

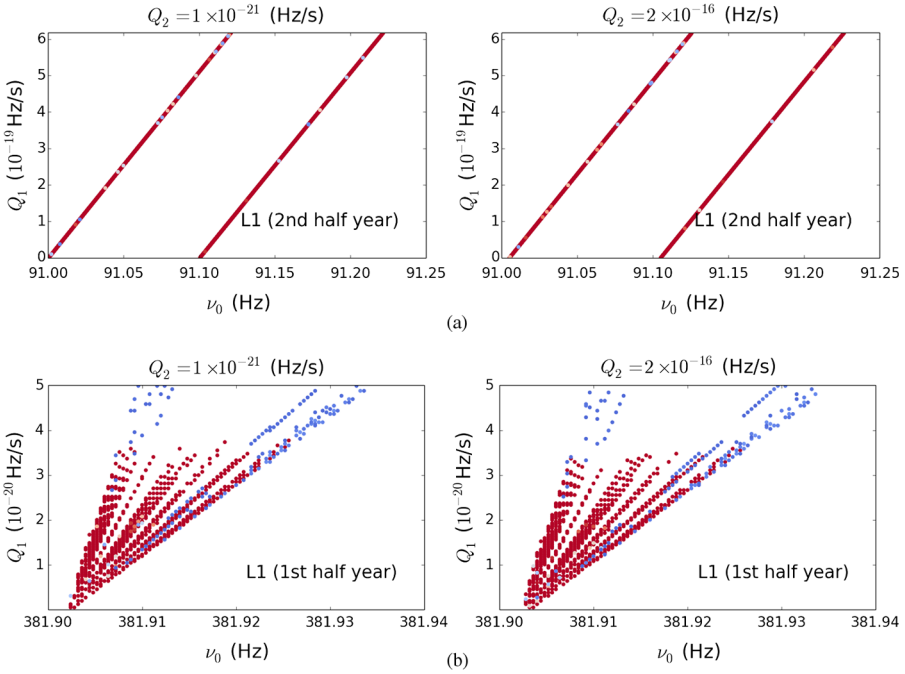

FIG. 19. Two strongest vetoed candidate clusters around (a) 91 Hz and (b) 381 Hz (both found in L1) seen in half of the second year of S5 data. The normalized detection statistic ρ/σ_ρ is plotted as a function of Q_1 and ν_0 for the two clusters. Each dot on the plots stands for one template $\{\nu_0, Q_1, Q_2\}$ with $\rho/\sigma_\rho > \rho_{\rm th} = 6.5$. The color of the dots indicates values of ρ/σ_ρ (larger ρ/σ_ρ in warmer colors). The cluster around 91 Hz only exists in the second half of the year (01 May 2007 to 30 October 2007 UTC). The cluster around 381 Hz only exists in the first half of the year (01 November 2006 to 30 April 2007 UTC). For each cluster, two values of Q_2 are searched: $Q_2 = 1 \times 10^{-21}$ Hz s^{-1} (left panels) and $Q_2 = 2 \times 10^{-16}$ Hz s^{-1} (right panels).

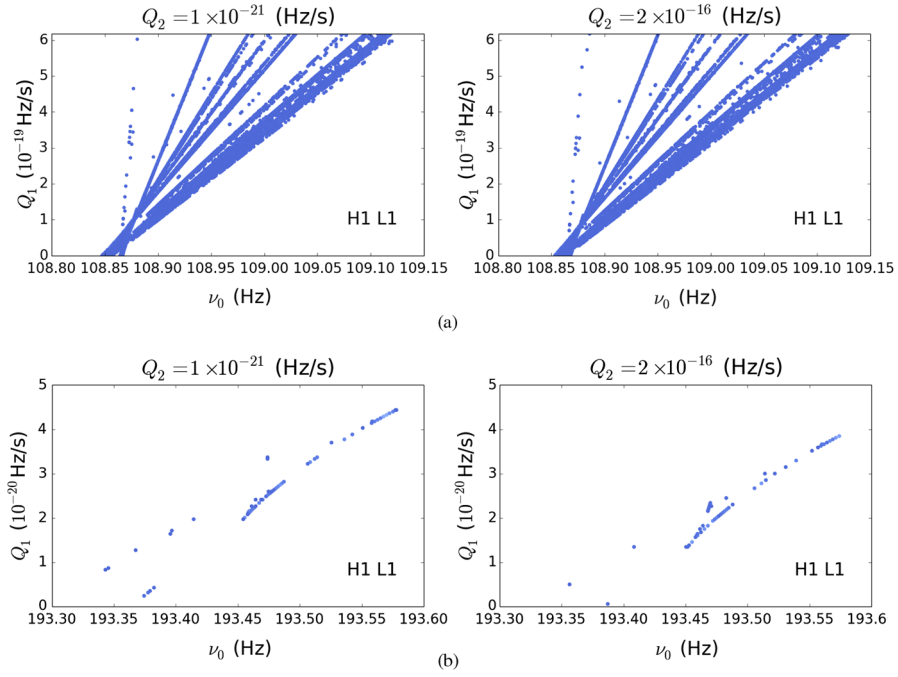

FIG. 20. Two examples of the clusters caused by instrumental lines at (a) 108.8 Hz and (b) 193.4 Hz. The normalized detection statistic ρ/σ_ρ is plotted as a function of Q_1 and ν_0. Each dot on the plots stands for one template $\{\nu_0, Q_1, Q_2\}$ with $\rho/\sigma_\rho > \rho_{\rm th} = 6.5$. For each cluster, two values of Q_2 are searched: $Q_2 = 1 \times 10^{-21}$ Hz s^{-1} (left panels) and $Q_2 = 2 \times 10^{-16}$ Hz s^{-1} (right panels). Both clusters are obtained from the second year of S5 data from two detectors (H1 and L1).

TABLE XVIII. Maximum Q_1 and Q_2 values in the two frequency bands of the search.

ν_0 range (Hz)	$Q_{1\max}$ (Hz s^{-1})	$Q_{2\max}$ (Hz s^{-1})
75–300	6.17×10^{-19}	2×10^{-16}
255–450	5×10^{-20}	2×10^{-16}

upper limit $h_0 \leq 3.8 \times 10^{-25}$ is obtained near 150 Hz with $Q_1 \leq 6.17 \times 10^{-19}$ Hz s^{-1} and $Q_2 \leq 2 \times 10^{-16}$ Hz s^{-1}.

Similarly, we also evaluate the upper limit on h_0 with $Q_1 = Q_2 = 0$ (i.e., $\dot{\nu} = 0$). We inject synthetic signals with $1 \times 10^{-25} \leq h_0 \leq 2 \times 10^{-24}$, $75 \leq \nu_0/\mathrm{Hz} \leq 450$, and $\dot{\nu} = 0$, plot the ρ/σ_ρ as contours on the (h_0, ν_0) plane, and draw the $\rho/\sigma_\rho = \rho_{\mathrm{th}} = 6.5$ curve, which represents the best upper limit achievable by the cross-correlation pipeline.

Figure 22 displays the comparison among the h_0 upper limits with the largest Q_1 and Q_2 (blue solid curves; same as red dashed curves in Fig. 21), the h_0 upper limits with $Q_1 = Q_2 = 0$ (green dash-dot curves), and the theoretical sensitivity from Eq. (31) (red dashed curves). The band is separated into the same two segments as in Fig. 21. For $\nu_0 \leq 150$ Hz, the blue curve and green curve almost overlap because we have $|\dot{\nu}(0)| \lesssim 10^{-7}$ Hz s^{-1} for all (Q_1, Q_2), and the pipeline tracks the signal phase accurately with an error $\lesssim 10^{-8}$ over a year. For $\nu_0 \gtrsim 150$ Hz, the

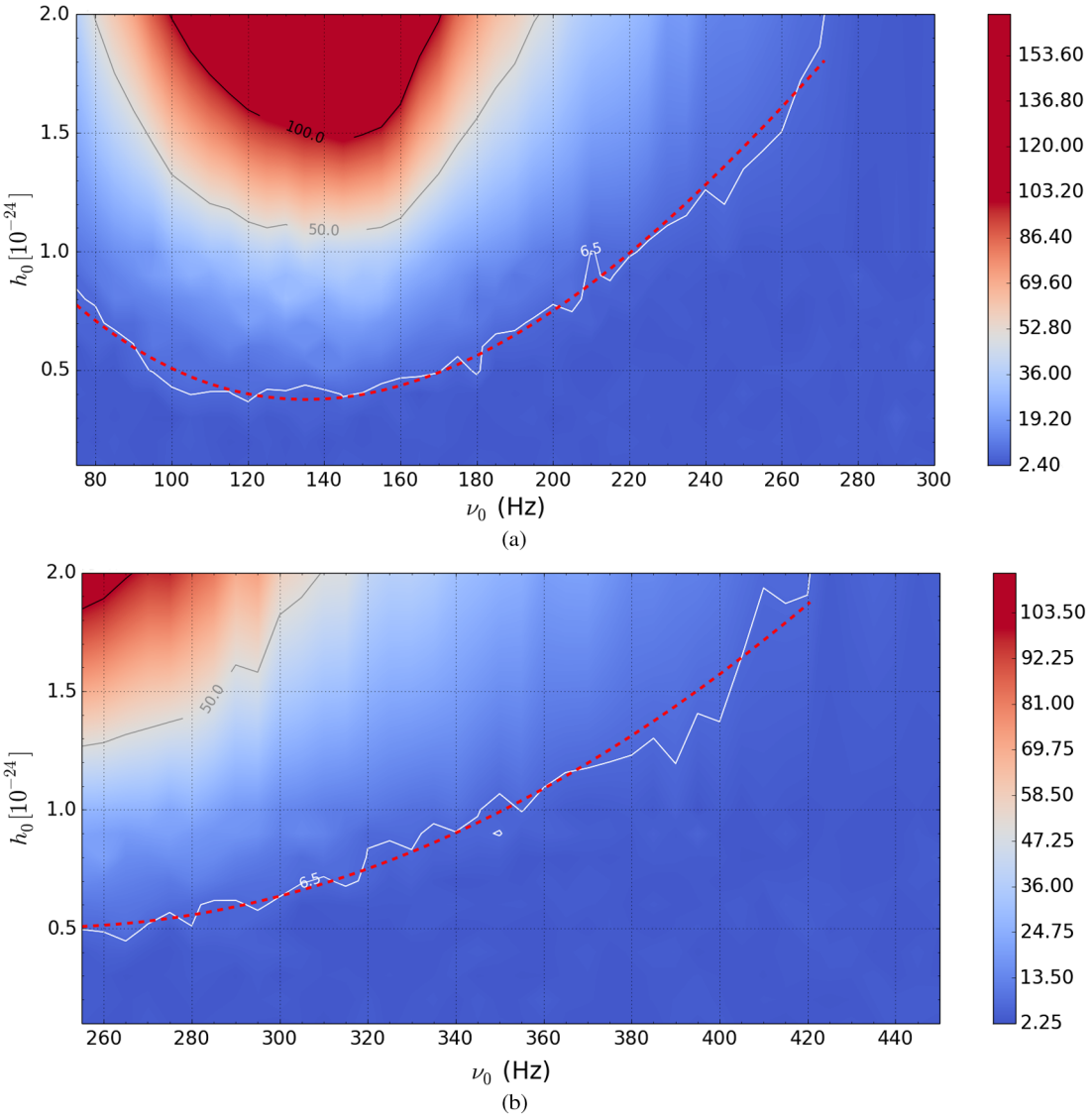

FIG. 21. Contours of normalized detection statistic ρ/σ_ρ from searching the synthetic data with different values of h_0 and ν_0 injected. The signals are generated with $1 \times 10^{-25} \leq h_0 \leq 2 \times 10^{-24}$ and (a) $75 \leq \nu_0/\mathrm{Hz} \leq 300$, $Q_1 = 6.17 \times 10^{-19}$ Hz s^{-1}, $Q_2 = 2 \times 10^{-16}$ Hz s^{-1}, and (b) $255 \leq \nu_0/\mathrm{Hz} \leq 450$, $Q_1 = 5 \times 10^{-20}$ Hz s^{-1}, $Q_2 = 2 \times 10^{-16}$ Hz s^{-1}. The red dashed curves are the contours $\rho/\sigma_\rho = \rho_{\mathrm{th}} = 6.5$, implying the 90% confidence level upper limit on h_0. The best upper limit $h_0 \leq 3.8 \times 10^{-25}$ is obtained near 150 Hz with $Q_1 \leq 6.17 \times 10^{-19}$ Hz s^{-1} and $Q_2 \leq 2 \times 10^{-16}$ Hz s^{-1}.

TABLE XIX. Parameter domain with sensitivity $h_0 \leq 8 \times 10^{-25}$ for the search in Sec. VI. The corresponding astrophysical parameters ϵ and B in Eq. (17) are quoted in the last column.

Search parameter	Range	Astrophysical parameter
ν_0	75–200 Hz	
Q_1	$2 \times 10^{-22} - 6.17 \times 10^{-19}$ Hz s^{-1}	$1.08 \times 10^{-5} \leq \epsilon \leq 6.0 \times 10^{-4}$
Q_2	$1 \times 10^{-21} - 2 \times 10^{-16}$ Hz s^{-1}	$4.05 \times 10^{9} \leq B/\mathrm{G} \leq 1.81 \times 10^{12}$

difference between upper limits with the largest Q_1 and Q_2 and upper limits with $Q_1 = Q_2 = 0$ increases with ν_0. If we diminish the Q_1 and Q_2 parameter space being searched, the corresponding upper limits with the largest Q_1 and Q_2 (blue curves) get closer to the green curves. Hence, the real h_0 upper limits always lie between the blue curves and green curves for the parameter space listed in Table XV. As a reference, the sensitivity in theory from Eq. (31) is plotted as red dashed curves in Fig. 22. It is $\sim 2 \times 10^{-25}$ to 4×10^{-25} lower than the best upper limits from the green curves. The discrepancy arises in at least two ways. First, the theoretical calculation pertains to the special case where $N_{\mathrm{pairs}} = 10^5$ and the noise floor in all SFTs is the same (see Sec. IV in Ref. [12] and Sec. IV.1 in Ref. [8]). Second, Eq. (31) is valid under the assumption that ρ is normally distributed (i.e., all SFT pairs are independent), which is not true in reality. From the analysis in Sec. IV A, the moments of the noise-only PDF of ρ/σ_ρ agree with those of a Gaussian distribution to an accuracy of over 95% for $T_{\mathrm{obs}} = 1$ yr. Hence, we do not expect the latter cause to contribute more than ~5% to the overall discrepancy, consistent with the discrepancy between the theoretical and empirical values of ρ_{th} in Sec. V A. A more accurate statistical investigation lies outside the scope of this paper.

Upper limits on ellipticity ϵ can be deduced from the h_0 upper limits (with the largest Q_1 and Q_2) in Figs. 21 and 22, using the relationship between wave strain at the Earth and the ellipticity of the star described in Eq. (30), and are plotted in Fig. 23 as blue curves. The dashed horizontal lines indicate the largest ϵ (see Table XV) searched in each panel, with $\epsilon = 6.0 \times 10^{-4}$ (left) and 1.71×10^{-4} (right). The upper limits on ϵ derived from h_0 are larger than the maximum values being searched, which indicates that the upper limits are still above the largest spin-down rate we are

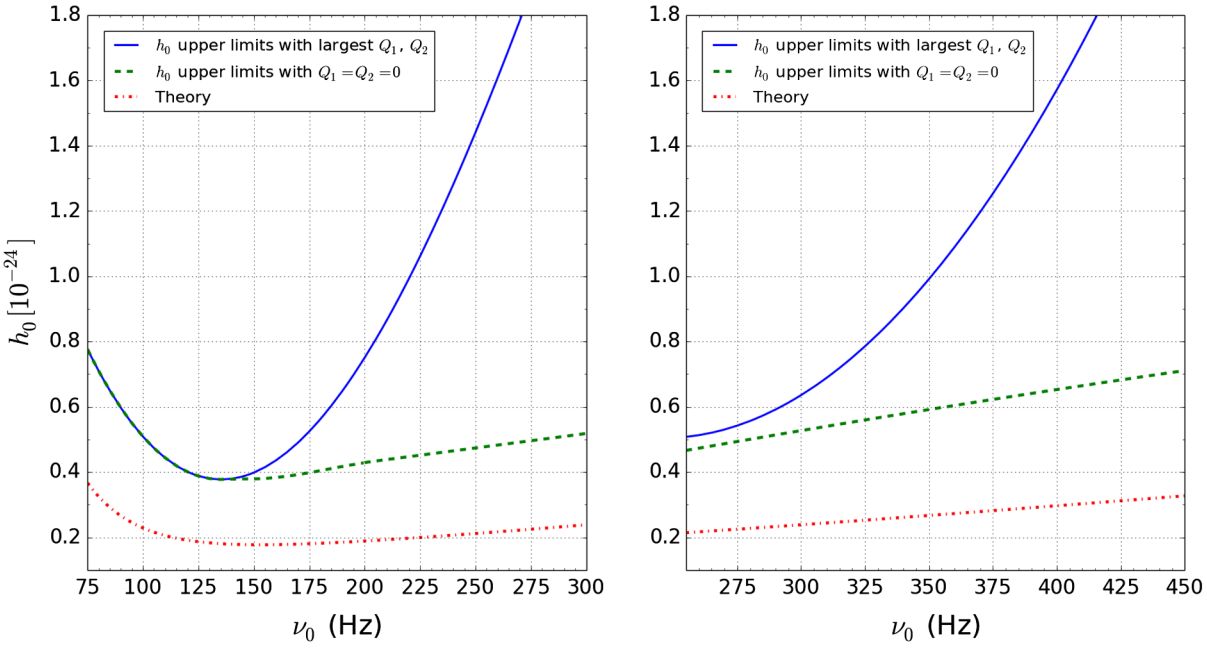

FIG. 22. Comparison among the h_0 upper limits with the largest Q_1 and Q_2 (blue solid curves), the h_0 upper limits with $Q_1 = Q_2 = 0$ (green dash-dot curves), and the theoretical sensitivity from Eq. (31) (red dashed curves). The left panel shows the band $75 \leq \nu_0/\mathrm{Hz} \leq 300$ with $Q_1 = 6.17 \times 10^{-19}$ Hz s^{-1} and $Q_2 = 2 \times 10^{-16}$ Hz s^{-1} injected for the blue curve. The right panel shows the band $255 \leq \nu_0/\mathrm{Hz} \leq 450$ with $Q_1 = 5 \times 10^{-20}$ Hz s^{-1} and $Q_2 = 2 \times 10^{-16}$ Hz s^{-1} injected for the blue curve. For $\nu_0 \leq 150$ Hz, the blue curve and green curve almost overlap because we have $|\dot{\nu}(0)| \lesssim 10^{-7}$ Hz s^{-1} for all (Q_1, Q_2), and the pipeline tracks the signal phase accurately with an error $\lesssim 10^{-8}$ over a year. The best upper limit $h_0 \leq 3.8 \times 10^{-25}$ is obtained near 150 Hz with $Q_1 \leq 6.17 \times 10^{-19}$ Hz s^{-1} and $Q_2 \leq 2 \times 10^{-16}$ Hz s^{-1}.

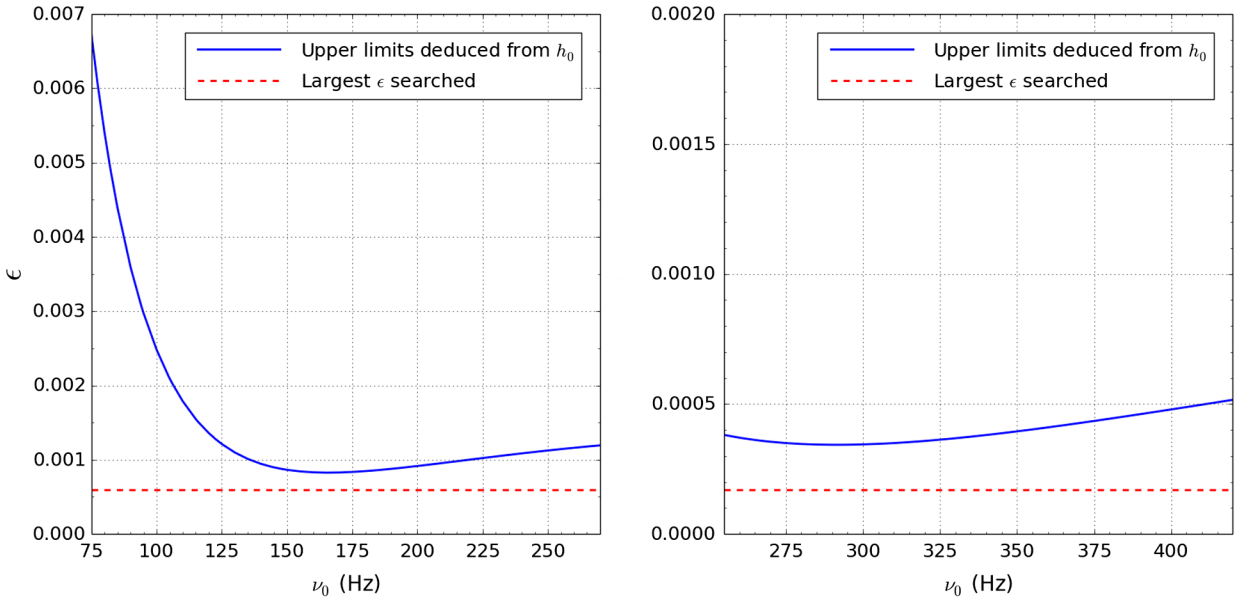

FIG. 23. Upper limits on ellipticity ϵ deduced from the h_0 upper limits (with the largest Q_1 and Q_2) using Eq. (30). The left and right panels are for the bands $75 \le \nu_0/\mathrm{Hz} \le 300$ and $255 \le \nu_0/\mathrm{Hz} \le 450$, respectively. The dashed horizontal lines indicate the largest ϵ searched in each panel, with $\epsilon = 6.0 \times 10^{-4}$ (left) and 1.71×10^{-4} (right). The best upper limit $\epsilon \le 8.2 \times 10^{-4}$ is obtained near 150 Hz, ~35% higher than the largest ellipticity being searched.

sensitive to. The best upper limit $\epsilon \le 8.2 \times 10^{-4}$ is obtained near 150 Hz, ~35% higher than the largest ellipticity being searched.

VII. CONCLUSION

In this paper, we perform a cross-correlation search for SNR 1987A using the second year of LIGO science run 5 data. The frequency band 75–450 Hz is searched. Six out of the total 19 first-pass candidates survive line vetoes. One out of the six second-pass candidates remains after the first stage of manual veto (searching two interferometers separately) but does not survive the second stage (searching first year of S5). With zero survivors, a 90% confidence level upper limit is placed on the wave strain given by $h_0 \approx 3.8 \times 10^{-25}$ at 150 Hz, the most sensitive frequency, corresponding to $\epsilon \approx 8.2 \times 10^{-4}$. The previous most sensitive search for SNR 1987A conducted with the radiometer pipeline yielded a 90% confidence level upper limit on the wave strain of $h_0 \approx 1.57 \times 10^{-24}$ (converted from the original value by the correction factor [59]) at the most sensitive frequency range [58]. Hence, the strain upper limit yielded from our search improves on previously published results by a factor ≈4.

To verify the algorithm, we conduct a battery of tests on synthetic data and verify that the cross-correlation data analysis pipeline is functioning correctly for gravitational-wave signals from a continuous-wave source obeying the spin-down law described by Eq. (17). It is demonstrated that averaging over $\cos\iota$ and ψ sacrifices typically $\lesssim$10% and at worst $\lesssim$50% sensitivity while delivering computational savings. It is also shown that the electromagnetic braking index n_{em} can be excluded from the search parameters (by setting $n_{\mathrm{em}} = 3$) without sacrificing sensitivity, alleviating concerns expressed in previous work [8]. We estimate the detection threshold and sensitivity with a group of Monte Carlo tests. Without spin-down, the estimated strain limits are $h_0^{95\%} \approx 5.64 \times 10^{-25}$, 7.60×10^{-25}, and 1.42×10^{-24} for 150, 300, and 600 Hz, respectively.

The next step in this investigation is to search Advanced LIGO data, as they become available. Despite a shorter observation period of 4 months for the first Advanced LIGO science run O1 (i.e., a threefold reduction in N_{pairs}), the noise power spectral density of Advanced LIGO is ~4 times better than Initial LIGO. Hence, referring to Eq. (31), we can expect improvement in the theoretical sensitivity h_{th}. On the other hand, the remnant has aged since S5, so the expected signal amplitude is lower in O1.

ACKNOWLEDGMENTS

We are grateful to Keith Riles, John Whelan, Badri Krishnan, Karl Wette, Benjamin Owen, and the LIGO Scientific Collaboration Continuous Wave Working Group for informative discussions. We are also grateful to Eric Thrane, Alberto Vecchio, and Teviet Creighton for their comprehensive formal review of the computer code and validation results of the SN1987A cross-correlation pipeline. L. S. is supported by an Australian Postgraduate Award. The research was supported by Australian

Research Council (ARC) Discovery Project No. DP110103347. P. D. L. is also supported by ARC DP140102578. Computations were done on the ATLAS Hannover cluster operated by the Albert Einstein Institute in support of research conducted by the LIGO and Virgo Scientific Collaborations, and the Pawsey Supercomputing Centre supported by the Australian Government and the Government of Western Australia.

[1] B. Abbott *et al.*, Phys. Rev. D **76**, 082001 (2007).
[2] B. Knispel and B. Allen, Phys. Rev. D **78**, 044031 (2008).
[3] K. Riles, Prog. Part. Nucl. Phys. **68**, 1 (2013).
[4] C. Peralta, A. Melatos, M. Giacobello, and A. Ooi, Astrophys. J. **644**, L53 (2006).
[5] A. Melatos and C. Peralta, Astrophys. J. **709**, 77 (2010).
[6] A. Melatos, Astrophys. J. **761**, 32 (2012).
[7] P. D. Lasky, Pub. Astron. Soc. Aust. **32**, e034 (2015).
[8] C. T. Y. Chung, A. Melatos, B. Krishnan, and J. T. Whelan, Mon. Not. R. Astron. Soc. **414**, 2650 (2011).
[9] P. R. Brady and T. Creighton, Phys. Rev. D **61**, 082001 (2000).
[10] B. Krishnan, A. M. Sintes, M. A. Papa, B. F. Schutz, S. Frasca, and C. Palomba, Phys. Rev. D **70**, 082001 (2004).
[11] B. Abbott *et al.*, Phys. Rev. D **77**, 022001 (2008).
[12] S. Dhurandhar, B. Krishnan, H. Mukhopadhyay, and J. T. Whelan, Phys. Rev. D **77**, 082001 (2008).
[13] K. Wette, Phys. Rev. D **92**, 082003 (2015).
[14] B. Abbott *et al.* (LIGO Scientific Collaboration), Rep. Prog. Phys. **72**, 076901 (2009).
[15] LIGO Scientific Collaboration and Virgo Collaboration, arXiv:1203.2674.
[16] B. Abbott *et al.* (LIGO Scientific Collaboration), Astrophys. J. Lett. **683**, L45 (2008).
[17] B. Abbott *et al.* (LIGO Scientific Collaboration), Astrophys. J. **713**, 671 (2010).
[18] B. Abbott *et al.* (LIGO Scientific Collaboration), Astrophys. J. **713**, 671 (2010).
[19] K. Wette *et al.*, Classical Quantum Gravity **25**, 235011 (2008).
[20] J. Abadie *et al.*, Astrophys. J. **722**, 1504 (2010).
[21] J. Aasi *et al.*, Astrophys. J. **785**, 119 (2014).
[22] J. Aasi *et al.*, Astrophys. J. **813**, 39 (2015).
[23] B. Abbott *et al.* (LIGO Scientific Collaboration), Phys. Rev. Lett. **102**, 111102 (2009).
[24] B. Abbott *et al.* (LIGO Scientific Collaboration), Phys. Rev. D **80**, 042003 (2009).
[25] J. Aasi *et al.*, Phys. Rev. D **90**, 062010 (2014).
[26] N. Panagia, Chin. J. Astron. Astrophys. Suppl. **8**, 155 (2008).
[27] R. N. Manchester, *Supernova 1987A: 20 Years After: Supernovae and Gamma-Ray Burste*, edited by S. Immler, K. Weiler, and R. McCray, *American Institute of Physics Conference Series* (AIP, New York, 2007), Vol. 937.
[28] J. T. Whelan, S. Sundaresan, Y. Zhang, and P. Peiris, Phys. Rev. D **91**, 102005 (2015).
[29] C. Messenger, H. Bulten, S. Crowder, V. Dergachev, D. Galloway, E. Goetz, R. Jonker, P. Lasky, G. Meadors, A. Melatos *et al.*, Phys. Rev. D **92**, 023006 (2015).
[30] E. V. Gotthelf, J. P. Halpern, C. Bassa, Z. Wang, A. Cumming, and V. M. Kaspi, in *AIP Conference Proceedings* (AIP, New York, 2008), Vol. 983, pp. 320–324.
[31] W. D. Arnett, J. N. Bahcall, R. P. Kirshner, and S. E. Woosley, Annu. Rev. Astron. Astrophys. **27**, 629 (1989).
[32] P. Podsiadlowski, Publ. Astron. Soc. Pac. **104**, 717 (1992).
[33] M. Aglietta *et al.*, Europhys. Lett. **3**, 1315 (1987).
[34] K. Hirata, T. Kajita, M. Koshiba, M. Nakahata, and Y. Oyama, Phys. Rev. Lett. **58**, 1490 (1987).
[35] R. M. Bionta, G. Blewitt, C. B. Bratton, D. Caspere, and A. Ciocio, Phys. Rev. Lett. **58**, 1494 (1987).
[36] J. N. Bahcall, A. Dar, and T. Piran, Nature (London) **326**, 135 (1987).
[37] G. J. M. Graves *et al.*, Astrophys. J. **629**, 944 (2005).
[38] D. N. Burrows, E. Michael, U. Hwang, R. McCray, R. A. Chevalier, R. Petre, G. P. Garmire, S. S. Holt, and J. A. Nousek, Astrophys. J. Lett. **543**, L149 (2000).
[39] J. Middleditch, J. A. Kristian, W. E. Kunkel, K. M. Hill, R. D. Watson, R. Lucinio, J. N. Imamura, T. Y. Steiman-Cameron, A. Shearer, R. Butler *et al.*, New Astron. **5**, 243 (2000).
[40] R. D. Blandford and R. W. Romani, Mon. Not. R. Astron. Soc. **234**, 57P (1988).
[41] A. Reisenegger, arXiv:astro-ph/0307133.
[42] J. A. Pons, J. A. Miralles, and U. Geppert, Astron. Astrophys. **496**, 207 (2009).
[43] F. C. Michel, Mon. Not. R. Astron. Soc. **267**, L4 (1994).
[44] R. C. Duncan and C. Thompson, Astrophys. J. Lett. **392**, L9 (1992).
[45] A. Bonanno, V. Urpin, and G. Belvedere, Astron. Astrophys. **440**, 199 (2005).
[46] J. W. Hartman, D. Bhattacharya, R. Wijers, and F. Verbunt, Astron. Astrophys. **322**, 477 (1997).
[47] Z. Arzoumanian, D. F. Chernoff, and J. M. Cordes, Astrophys. J. **568**, 289 (2002).
[48] C.-A. Faucher-Giguère and V. M. Kaspi, Astrophys. J. **643**, 332 (2006).
[49] H. Ögelman and M. A. Alpar, Astrophys. J. Lett. **603**, L33 (2004).
[50] C. D. Ott, A. Burrows, T. A. Thompson, E. Livne, and R. Walder, Astrophys. J. Suppl. Ser. **164**, 130 (2006).
[51] T. Dotani, K. Hayashida, H. Inoue, M. Itoh, and K. Koyama, Nature (London) **330**, 230 (1987).
[52] H. Inoue, K. Hayashida, M. Itoh, H. Kondo, K. Mitsuda, T. Takeshima, K. Yoshida, and Y. Tanaka, Publ. Astron. Soc. Jpn. **43**, 213 (1991).
[53] C. Palomba, Mon. Not. R. Astron. Soc. **359**, 1150 (2005).
[54] T. Piran and T. Nakamura, Prog. Theor. Phys. **80**, 18 (1988).
[55] T. Nakamura, Prog. Theor. Phys. **81**, 1006 (1989).

[56] K. Soida, M. Ando, N. Kanda, H. Tagoshi, D. Tatsumi, K. Tsubono, and the TAMA Collaboration, Classical Quantum Gravity **20**, S645 (2003).
[57] T. M. Niebauer, A. Rüdiger, R. Schilling, L. Schnupp, W. Winkler, and K. Danzmann, Phys. Rev. D **47**, 3106 (1993).
[58] J. Abadie *et al.*, Phys. Rev. Lett. **107**, 271102 (2011).
[59] C. Messenger, LIGO Document T1000195 (2011).
[60] G. Santostasi, W. Johnson, and J. Frank, Astrophys. J. **586**, 1191 (2003).
[61] A. Melatos, Mon. Not. R. Astron. Soc. **288**, 1049 (1997).
[62] I. Contopoulos and A. Spitkovsky, Astrophys. J. **643**, 1139 (2006).
[63] M. A. Livingstone, V. M. Kaspi, F. P. Gavriil, R. N. Manchester, E. V. G. Gotthelf, and L. Kuiper, Astrophys. Space Sci. **308**, 317 (2007).
[64] P. Jaranowski, A. Królak, and B. F. Schutz, Phys. Rev. D **58**, 063001 (1998).
[65] R. Prix and J. T. Whelan, Classical Quantum Gravity **24**, S565 (2007).
[66] J. Arons, arXiv:0708.1050.
[67] W. Feller, *An Introduction to Probability Theory and Its Applications* (Wiley, New York, 1957).
[68] T. Damour, B. R. Iyer, and B. S. Sathyaprakash, Phys. Rev. D **63**, 044023 (2001).
[69] R. Coyne, A. Corsi, and B. J. Owen, Phys. Rev. D **93**, 104059 (2016).
[70] B. Tabachnick and L. Fidell, *Using Multivariate Statistics* (Harper & Row, New York, 1996).
[71] J. Aasi *et al.*, Phys. Rev. D **87**, 042001 (2013).